Advanced Healthcare Materials

ADVANCED HEALTHCARE MATERIALS
www.advhealthmat.de

RESEARCH ARTICLE OPEN ACCESS

Macrophage Membrane-Cloaked, ROS-Triggered Quercetin Nanocarriers Target Ovarian Lesions to Treat Polycystic Ovary Syndrome

Wenzhu Li[1] | Yu Guan[1] | Nan Song[2] | Feng Zhang[1] | Zhimin Deng[1] | Tailang Yin[1] | Yanbing Yang[2] | João Conde[3] | Wenyi Jin[4,5] | Zhinang Yin[6]

[1]Reproductive Medicine Center, Renmin Hospital of Wuhan University, Wuhan University, Wuhan, China | [2]College of Chemistry and Molecular Sciences, Key Laboratory of Biomedical Polymers of Ministry of Education, Institute of Molecular Medicine, Renmin Hospital of Wuhan University, Wuhan University, Wuhan, China | [3]Comprehensive Health Research Centre (CHRC), NOVA Medical School, Faculdade de Ciências Médicas, NMS| FCM, Universidade NOVA de Lisboa, Lisboa, Portugal | [4]Department of Orthopaedics, Renmin Hospital of Wuhan University, Wuhan University, Wuhan, China | [5]Department of Biomedical Sciences, City University of Hong Kong, Hong Kong, China | [6]Department of Clinical Laboratory, Renmin Hospital of Wuhan University, Wuhan, China

Correspondence: Tailang Yin (reproductive@whu.edu.cn) | Yanbing Yang (yangyanbing@whu.edu.cn) | João Conde (joao.conde@nms.unl.pt) | Wenyi Jin (gin1994@whu.edu.cn) | Zhinang Yin (yinzhinang@whu.edu.cn)

Received: 16 October 2025 | **Revised:** 23 January 2026 | **Accepted:** 10 February 2026

Keywords: biomimetic nanomaterials | granulosa cells | polycystic ovary syndrome | reactive oxygen species | ROS-responsive

ABSTRACT

Polycystic ovary syndrome (PCOS) involves oxidative stress-driven ovarian dysfunction and remains difficult to treat due to drug side effects and poor target engagement. We engineered a reactive oxygen species (ROS)-responsive, macrophage-membrane-camouflaged quercetin nano-therapy (MM@PCD@QNPs) to enhance ovarian delivery and mitigate toxicity. The core comprises a pinacol phenylboronate-dextran conjugate that encapsulates quercetin and undergoes ROS-triggered release; a surface M0 macrophage membrane confers immune evasion and lesion tropism via retained proteins (e.g., CD11b and CD47-SIRPα). MM@PCD@QNPs displayed nanoscale dimensions and stability (133.63 $\pm$ 14.60 nm; -33.13 ± 1.52 mV) and released drug under elevated ROS. In DHT-injured granulosa cells and a DHEA-induced PCOS mouse model, the formulation promoted granulosa cell proliferation, suppressed apoptosis, reduced ROS, and preferentially accumulated in ovaries, with negligible in vitro and in vivo toxicity. Transcriptomics and validation implicate activation of the MAPK7-Nrf2-NQO1 axis as a principal mechanism; pharmacologic MAPK7 inhibition abrogated therapeutic effects. By coupling ROS-triggered release with macrophage-mimetic targeting, MM@PCD@QNPs overcome quercetin's low bioavailability and off-target exposure and provide a safe, effective nanoplatform for PCOS therapy.

1 | Introduction

Polycystic ovary syndrome (PCOS) is a prevalent young-set reproductive endocrine disorder, affecting up to one in five women of childbearing age [1]. Defined by ovulatory dysfunction, hyperandrogenism, and polycystic ovarian morphology, PCOS is frequently accompanied by insulin resistance, dysmetabolism, and adverse pregnancy outcomes [1, 2]. Current therapies (hormonal modulation, antiandrogens, insulin sensitizers) alleviate symptoms but carry adverse effects, show

Wenzhu Li, Yu Guan, and Nan Song contributed equally to this work.

variable long-term efficacy, and offer limited disease modification.

Converging evidence implicates oxidative stress (OS), excessive reactive oxygen species (ROS) and impaired antioxidant defenses, as a central driver of granulosa-cell dysfunction, follicular arrest, mitochondrial injury, and ferroptosis [3–6]. Some natural plant extracts and Chinese traditional medicines have shown great potential in recuperation PCOS [7]. Quercetin (QUR), a dietary flavonoid, shows broad antioxidant and anti-inflammatory activity and has improved endocrine and ovarian phenotypes in PCOS models [8–10]. However, its clinical translation is restricted by unfavorable aqueous solubility, rapid metabolism, and low oral bioavailability, necessitating high doses that increase systemic exposure and reduce ovarian targeting [11]. These limitations motivate formulation strategies that both boost bioavailability and deliver quercetin to ovarian tissue while limiting off-target toxicity [12].

Functional nanomaterials overcome the inherent limitations of small molecule antioxidants to some extent. For example, melatonin-loaded polydopamine nanoparticles were used as ROS scavengers for the treatment of dry eye syndrome [13]. Resveratrol-loaded cerium dioxide nano-enzymes significantly improved hormone disruption and inflammation in dehydroepiandrosterone (DHEA)-induced PCOS mice [14]. Boron esters are reported to be oxidatively unstable in response to ROS, aiding in targeted drug release at disease sites [15–17]. Normally, 4-(hydroxymethyl) phenylboronic acid pinacol ester (PBAP) is stable, with its hydrophobic pinacol group protecting against hydrolysis. However, in the presence of excess free radicals, it facilitates borate bond cleavage, neutralizes ROS [18], which is often used as an antioxidant prodrug [17, 19, 20] due to its mild chemical reaction, easy conjugation, and low toxicity of metabolites. Therefore, the nanomaterials constructed by borate-modified polymers have stable ROS response effects. Despite extensive advances in the application of these materials, clinical approval is limited, mainly due to concerns related to biosafety, complexity of synthesis processes, and high costs.

Recently, biomimetic nanoparticle delivery systems based on cell membranes or micro-vesicles exhibited promising potential in treating various diseases, including diabetes, non-alcoholic fatty liver disease, and anti-atherosclerosis [21–23] due to their high biocompatibility and plasticity, lesion targeting, and excellent immune evasion properties [24]. For example, red blood cell membrane-encapsulated nanoparticles could prolong blood circulation and reduce immunogenicity [25], while macrophage membrane-encapsulated nanoparticles specifically target inflammation and cancer lesions, avoiding clearance by the immune system and reducing drug toxicity and side effects [21]. However, the application of this technology in the treatment of gynecological diseases, especially PCOS, remains unexplored.

Given the central role of oxidative stress in PCOS pathogenesis, this study utilized macrophage membranes and pinacol phenylboronic acid ester to develop a macrophage membrane-encapsulated ROS-responsive biomimetic nanoparticle delivery system loaded with QUR, to overcome the limitations of traditional QUR administration, and achieve precise targeting of polycystic ovary inflammatory lesions, representing an efficient and safe innovative treatment strategy for the clinical treatment of PCOS.

2 | Results

2.1 | Synthesis Process of MM@PCD@QNPs and Its Stable Characterization

Network pharmacological analysis identified QUR as the promising ROS-responsive compound in treating PCOS (Figure S1). To facilitate its clinical translation, we developed a biomimetic nano-delivery system encapsulated within a macrophage membrane (MM). QUR-loaded PABP conjugated with dextran (DEX) polymer nanoparticles (PCD@QNPs) were fabricated using nanoprecipitation-dialysis across various PCD-to-QUR mass ratios (10:1, 5:1, 2:1, 1:1, and 1:2). Subsequent optimization of the MM coating was performed via ultrasonic hydration and liposomal extrusion at PCD@QNP-to-MM mass ratios of 100:1, 10:1, 1:1, and 1:10. Stability assessments showed that PCD@QNPs at 10:1 and 5:1 ratio maintained a stable, nanoscale size, whereas other ratios led to aggregation and precipitation (Figure 1A; Figure S2). The MM@PCD@QNPs at a 1:1 ratio demonstrated optimal stability in both size and zeta potential (Figure S3). The 5:1 PCD@QNPs were selected for further development, exhibiting a drug loading efficiency of 11.44 ± 0.84% and an encapsulation efficiency of 72.75 ± 2.79% (Figure 1B). These nanoparticles had a hydrodynamic size of 87.65 ± 4.14 nm and a zeta potential of -16.53 ± 0.90 mV. Coating with MM of equivalent quality increased the size to 133.63 ± 14.60 nm (Figure 1C) and shifted the zeta potential to -33.13 ± 1.52 mV (Figure 1D), reflecting the highly negative surface charge of the native membrane (-46.33 ± 2.00 mV). Given the high reactivity of aryl boronic esters with ROS, we investigated the drug release profile in response to hydrogen peroxide (H_2O_2) [26]. In a buffer containing 500 nM H_2O_2, PCD@QNPs released 69.69 ± 1.19% of QUR cumulatively over 7 days, significantly higher than the 58.00 ± 1.49% released in its absence. Under the same conditions, MM@PCD@QNPs showed cumulative release rates of 59.02 ± 1.49% and 53.86% ±1.22%, respectively (Figure 1E). which suggested H_2O_2 accelerated QUR liberation from the nanocarrier. The macrophage membrane coating has a certain delaying effect on ROS-responsive drug release. Figure S8 showed that MM@PCD@QNPs exhibited extremely high stability, with the lowest cumulative release rate at 24 h. The drug release amount of MM@PCD@QNPs was significantly increased under H_2O_2 condition, but still lower than that of non-MM coating NPs. The MM coating acted as a secondary barrier, slightly delaying release and providing a more controlled profile. These properties make MM@PCD@QNPs highly suitable for targeted drug delivery to the ROS-rich ovarian microenvironment in PCOS. Dynamic light scattering (DLS) in phosphate buffered saline (PBS) confirmed the strong colloidal stability of both formulations over three weeks, with PCD@QNPs degrading slightly earlier than their membrane-coated counterparts (Figure 1F).

Fourier transform infrared spectroscopy (FTIR) revealed a characteristic peak at 1748 cm^{-1} (ester group, C = O stretching vibration) for both the synthesized PCDs and PCD@QNPs, while the stretching vibration peak of the carbon-oxygen double bond (carbonyl group) on the phenyl ring of QUR was located at

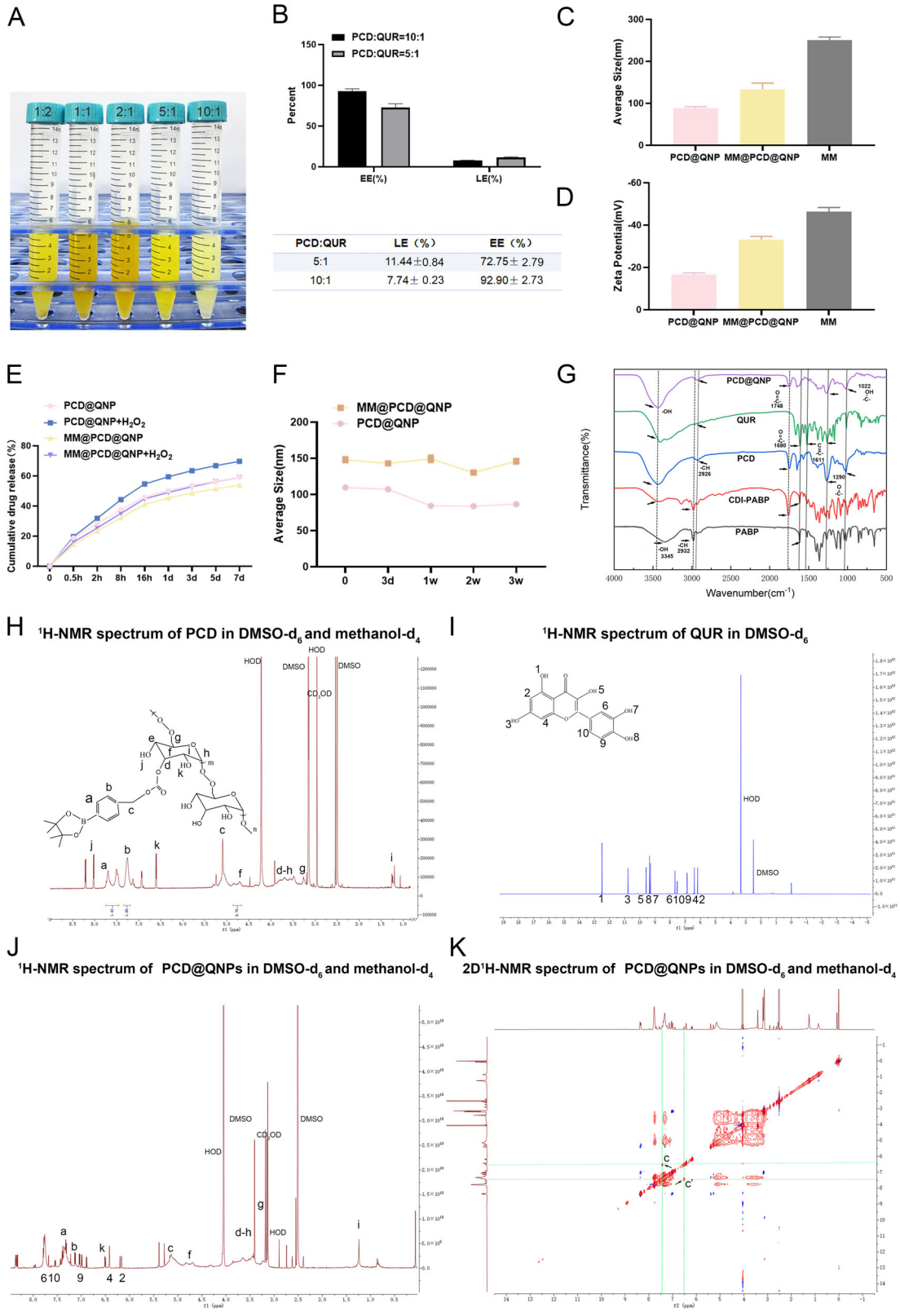

FIGURE 1 | Characterization of the prepared NPs. (A) Physical images of NPs with different PCD: QUR mass ratios. (B) Encapsulation and drug loading rates of two types of NPs (10:1 and 5:1). Size (C) and zeta potential. (E) Cumulative release rate of NPs with and without H_2O_2. (F) Dynamic size change of NPs. (G) Fourier infrared spectroscopy of NPs. (H) ^{1}H-NMR spectrum of PCD. (I) ^{1}H-NMR spectrum of QUR. (J) ^{1}H-NMR spectrum of PCD@QNPs. (K) 2D ^{1}H-NMR spectrum of PCD@QNPs, c and c' represented the displacement points of hydrogen bonds in symmetrical interactions.

approximately 1680 cm^{-1} (Figure 1G). Appropriate solvents based on the solubility of the substances were selected to perform proton nuclear magnetic resonance (^{1}H-NMR) investigating the intermolecular non-covalent interactions. PCDs were dissolved in deuterated dimethyl sulfoxide (DMSO) /methanol (v/v = 1:1). Due to interference from the solvent peaks, the PCDs proton spectrum was concentrated between 1–8.5 ppm, with the signals at 3–4 ppm attributed to the pyran ring protons. This assay verified PBAP was successfully grafted onto the hydroxyl groups of DEX via chemical coupling, with a grafting efficiency of 70%, forming the PCDs nanocore, despite solvent peak interference (Figure 1H). Figure 1I depicted the ^{1}H-NMR spectrum of QUR in deuterated DMSO, where signals >9 ppm corresponded to phenolic hydroxyl protons, while 6–8 ppm were attributed to aromatic ring hydrogens. Figure 1J showed that PCD@QNPs retained characteristic proton signals from both QUR and PCDs, but no phenolic hydroxyl peak was observed; PCDs exhibited no corresponding signals at 5.31–6.61 ppm, whereas QUR displayed aromatic ring hydrogens at 6.00–6.89 ppm. 2D ^{1}H-NMR (Figure 1K) further revealed a correlation between 7.25 and 6.17 ppm protons, suggesting their mutual interaction. The results indicated successful self-assembly via non-covalent interactions and multi-functional group coordination.

Characterization confirmed the integrity of the MM coating. Sodium dodecyl sulfate polyacrylamide gel electrophoresis (SDS-PAGE) demonstrated a protein profile for MM@PCD@QNPs similar to pure MM, and western blot analysis confirmed the presence of key surface proteins, including the M0 marker cluster of differentiation 11b (CD11b) and the immune evasion molecule signal regulatory protein α (SIRPα) (Figure 2A,B). Transmission electron microscope (TEM) revealed a spherical morphology for MM@PCD@QNPs, with a clearly visible MM layer encapsulating the nanoparticles (NPs) core, unlike the uncoated PCD@QNPs (Figure 2C). Previous studies have shown that immune cell membrane-mimetic NPs can evade capture by the monocyte-macrophage system, thereby reducing drug clearance [27–29]. In vitro uptake experiments showed that LPS-stimulated macrophages (murine macrophage cell line, Raw 264.7) phagocytosed dioctadecyl-3, 3, 39, 39-tetramethyl-1, 3-dicarboxycyanine perchlorate (DiD) labeled-nanoparticles (DNPs) readily, but significantly fewer macrophage membrane-coated DiD labeled-nanoparticles (MM@DNPs), compared with M0 cells (Figure 2D,E). Lipopolysaccharide (LPS)-induced Tsuchiya human monocytic leukemia cell line (THP-1) cells phagocytosed fewer MM@DNPs, with no significant difference compared with other groups (Figure S4A,B). Conversely, using a 500 nM dihydrotestosterone (DHT)-induced chronic inflammation [30], the uptake of MM@DNPs was significantly greater than that of DNPs in granulosa cells (primary mouse ovarian granulosa cells and human ovarian granulosa-like tumor cell line) (CP-M050 and KGN) (Figure 2F,G; Figure S4C, D) indicating enhanced targeting to the desired cells [31].

2.2 | The High Biosafety, Low Toxicity and Few Side Effects of MM@PCD@QNPs

Cytotoxicity was assessed to determine safe working concentrations. Cell Counting Kit-8 (CCK-8) assays established 500 nM DHT as a suitable in vitro intervention concentration (Figure S4E), consistent with several previous studies [32]. Treatment with MM@PCD@QNPs (10 ng/mL to 100 μg/mL) for 24 h showed no significant cytotoxicity in KGN cells, though reduced viability was observed at 1 μg/mL and 100 μg/mL after 48 h (Figure 3A). Consequently, 10 μg/mL was selected for subsequent in vitro studies. Live-dead staining corroborated that MM@PCD@QNPs components were non-toxic to KGN cells compared to DHT treatment alone (Figure 3D).

For in vivo safety, mice were intraperitoneally injected with MM@PCD@QNPs at concentrations of 1, 5, and 15 mg/mL at a rate of 3 μL per g of body weight (n = 3). Preliminary hemolysis analysis indicated concentration-dependent effects, with MM@PCD@QNPs exhibiting lower hemolysis rates than PCD@QNPs (Figure S4F,G). A concentration of 5 mg/mL was chosen for a two-week treatment in PCOS mice. At this dose, the hemolysis rate of all components was significantly lower than the positive control (H_2O), and MM@PCD@QNPs showed a lower rate than free QUR (Figure 3B,C). Analysis of serum biomarkers for liver (alanine aminotransferase, aspartate aminotransferase) (ALT, AST) and kidney (blood urea nitrogen, creatinine) (BUN, CRE) function revealed no significant abnormalities (Figure 3E–H), and hematoxylin and eosin (H&E) staining showed normal histology in the heart, liver, spleen, lung, kidney, and uterus (Figure 3I). Furthermore, MM@PCD@QNPs treatment counteracted the dyslipidemia characteristic of PCOS, normalizing serum levels of (triglyceride) TG, TC (total cholesterol), LDL (low-density lipoprotein), and HDL (high-density lipoprotein) (Figure 3J–M). These results collectively demonstrated the high biocompatibility and low systemic toxicity of the developed nanocomposites, which provided a potential therapeutic strategy for PCOS.

2.3 | MM@PCD@QNPs Improve Granulosa Cell Function in a Hyperandrogenic Environment by Promoting Proliferation, Inhibiting Apoptosis, and Reducing ROS Levels

Cell proliferation and apoptosis are key functions of granulosa cells in the ovary. 5-ethynyl-2′-deoxyuridine (EdU) staining revealed that 500 nM DHT for 24 h significantly suppressed KGN proliferation, an effect that was reversed by co-treatment with MM@PCD@QNPs (Figure 4A,B). CCK-8 assays confirmed that both QUR and MM@PCD@QNPs significantly promoted cell proliferation after 72 h (Figure 4C). Flow cytometry analysis demonstrated that MM@PCD@QNPs effectively attenuated DHT-induced apoptosis, showing the lowest percentages of early and total apoptotic cells (Figure 4D,E). This was consistent with a decreased ratio of Cleaved-Caspase3 to Caspase3 (C-CAS3/CAS3) (Figure 4F,G). The anti-apoptotic effect of the nano-formulation was more potent than free QUR at an equivalent concentration. Since mitochondrial dysfunction and OS are hallmarks of PCOS, we assessed the mitochondrial membrane potential using 5, 5′, 6, 6′-Tetrachloro-1, 1′, 3, 3′-tetraethylbenzimidazolylcarbocyanine iodide (JC-1) staining. The DHT group exhibited severe mitochondrial depolarization, which was significantly restored by MM@PCD@QNPs (Figure 4H,I).

Intracellular ROS levels, measured by 2′, 7′-dichlorodihydro fluorescein diacetate (DCFH-DA) fluorescence and flow cytom-

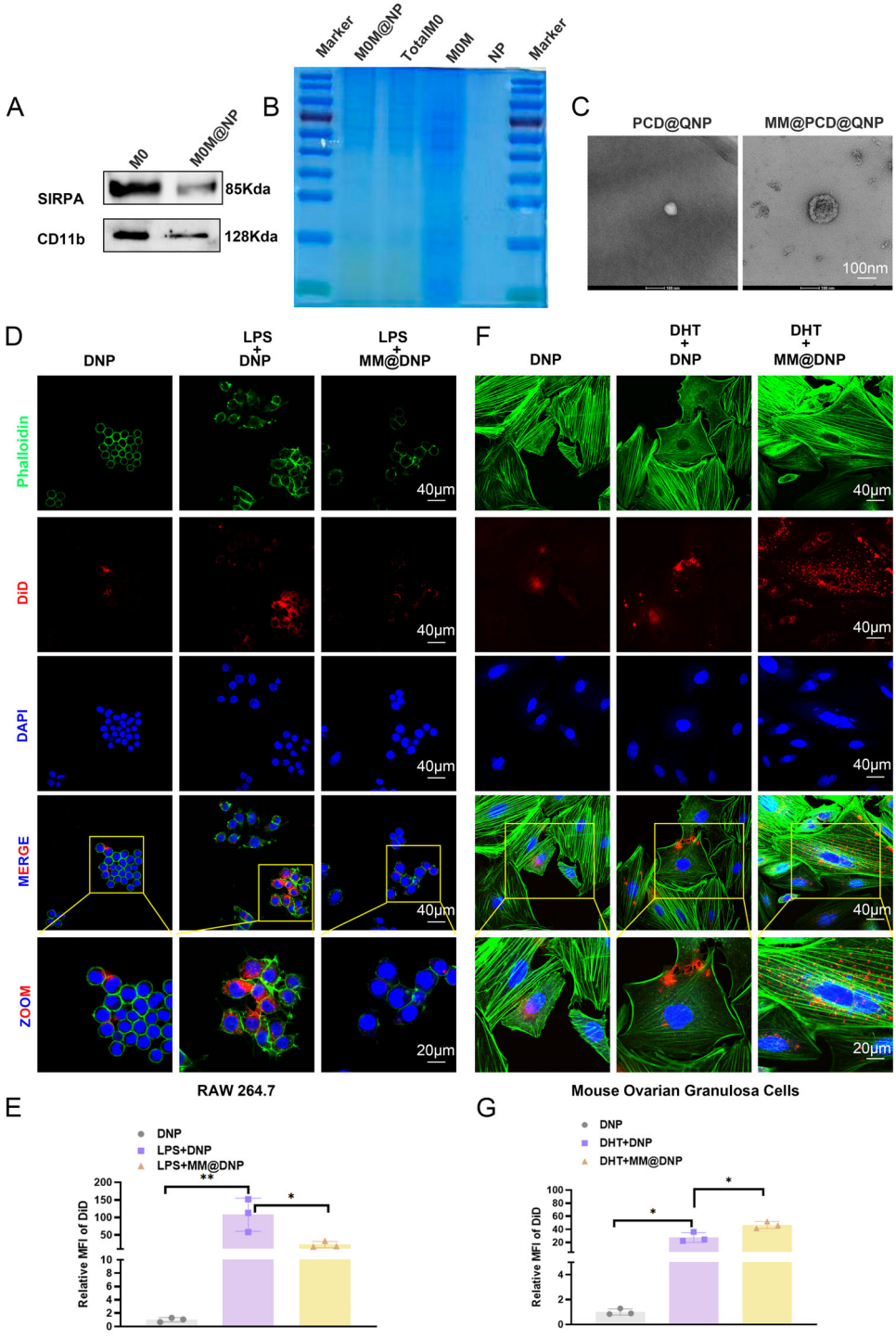

FIGURE 2 | Cell membrane characterization of the prepared NPs. (A) Key protein C11b and SIRPA validation and visualization (B) of NPs. (C) TEM images of NPs. Scale bar at 100 nM. (D) In vitro uptake of NPs by Raw 264.7 cells under LPS presence and absence with (E) statistical analyses. (F) In vitro uptake of NPs by primary mouse ovarian granulosa cells under DHT present and absent with (G) statistical analyses. The data were presented as mean ± SD, n = 3. One-way ANOVA with post hoc multiple comparisons, *p < 0.05, **p < 0.01.

etry, were markedly elevated by DHT but substantially reduced by MM@PCD@QNPs, with free QUR showing a more modest effect (Figure 5A–D). The activity of the antioxidant enzyme superoxide dismutase (SOD) was increased by PCDs, MM@PCDs, PCD@QNPs, and MM@PCD@QNPs, but only MM@PCD@QNPs significantly reduced the levels of malondialdehyde (MDA) (Figure 5E,F). Western blot analysis further showed that MM@PCD@QNPs significantly upregulated the expression of the antioxidant enzymes NAD(P)H:quinone oxidoreductase 1 and heme oxygenase-1 (NQO1 and HO-1) compared to the DHT group (Figure 5G,H), while the improvement effect of QUR at the same concentration was less significant. It also increased the protein expression of cytochrome p450 family 19 subfamily A member 1(CYP19A1), a key enzyme for estrogen

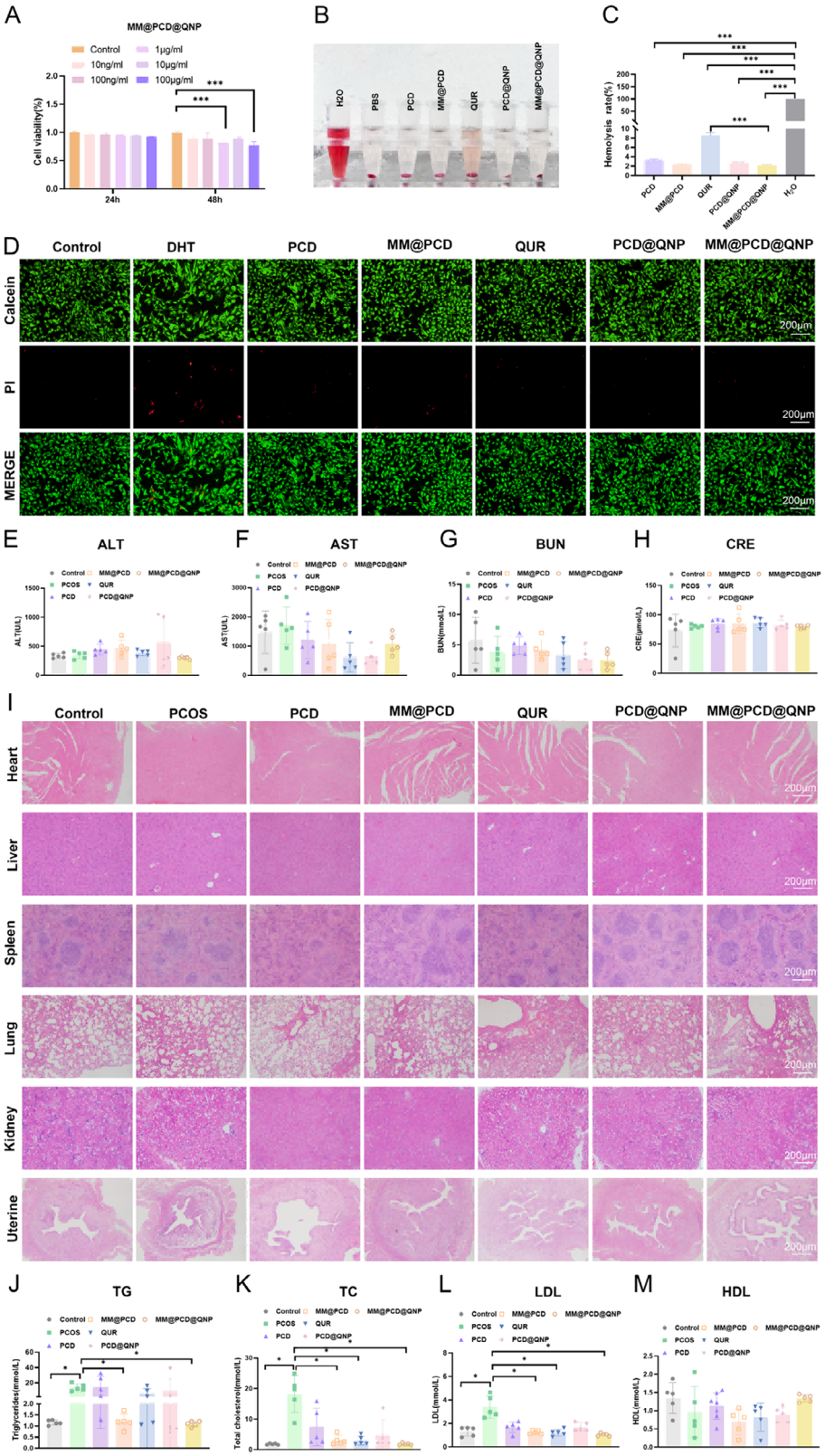

FIGURE 3 | Biosafety of the prepared NPs. (A) Cytotoxicity assay of MM@PCD@QNPs. n = 3. One-way ANOVA followed by post hoc multiple comparisons. (B) Images and (C) statistical analyses of hemolysis analysis for NPs. n = 3. One-way ANOVA followed by post hoc multiple comparisons. (D) Cell viability staining of NPs, with green indicating Calcein and red indicating PI, scale bar is 200 μM. Biochemical analysis of mouse serum ALT (E), AST (F), BUN (G), and CRE (H) after NPs treatment. n = 5. Corrected Brown-Forsythe and Welch tests with post hoc multiple comparisons. (I) H&E staining of heart, liver, spleen, lung, kidney, and uterus (scale bar = 200 μM) after NPs treatment. Biochemical analysis of mouse serum TG (J), TC (K), LDL(L), and HDL (M) after NPs treatment. Corrected Brown-Forsythe and Welch tests with post hoc multiple comparisons. The data were presented as mean ± SD.*$p < 0.05$, ***$p < 0.001$.

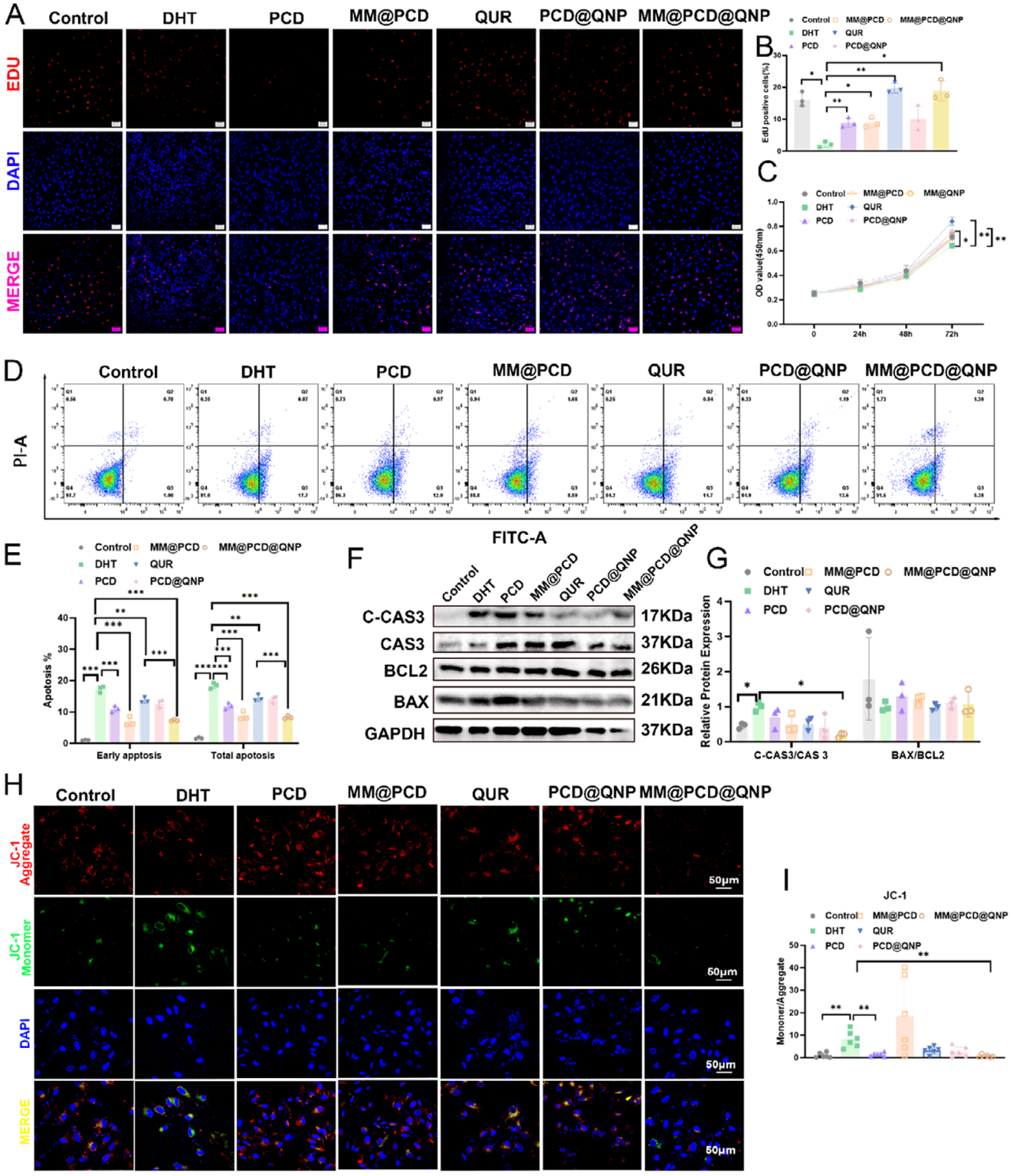

FIGURE 4 | Effects of the prepared NPs on the proliferation and apoptosis of granulosa cells. After different NPs treatment, (A) Edu staining and (B) statistical analyses, with red representing proliferative cells and blue representing DAPI, scale bar at 50 μM. n = 3. Corrected Brown-Forsythe and Welch tests with post hoc multiple comparisons. (C) CCK8 analysis, plotted using OD values. n = 3. One-way ANOVA followed by post hoc multiple comparisons. Flow cytometry visualization (D) and (E) statistics of apoptosis; the x-axis represents the FITC channel, the y-axis represents the PI channel, FITC positive and PI negative indicate early apoptotic cells, FITC and PI double positive indicate necrotic cells, the sum of both indicates total apoptotic cells. n = 3. Two-way ANOVA followed by post hoc multiple comparisons. (F) Key apoptotic proteins (C-CAS3/CAS3, BAX and BCL2) and (G) statistical analyses. n = 3. Corrected Brown-Forsythe and Welch tests with post hoc multiple comparisons. (H) JC-1 staining and (I) statistics, with red indicating aggregates, green indicating monomers, blue representing DAPI, scale bar at 50 μM. n = 6. Nonparametric Kruskal-Wallis test with post hoc multiple comparisons. The data were presented as mean ± SD.*p < 0.05, **p < 0.01, ***p < 0.001.

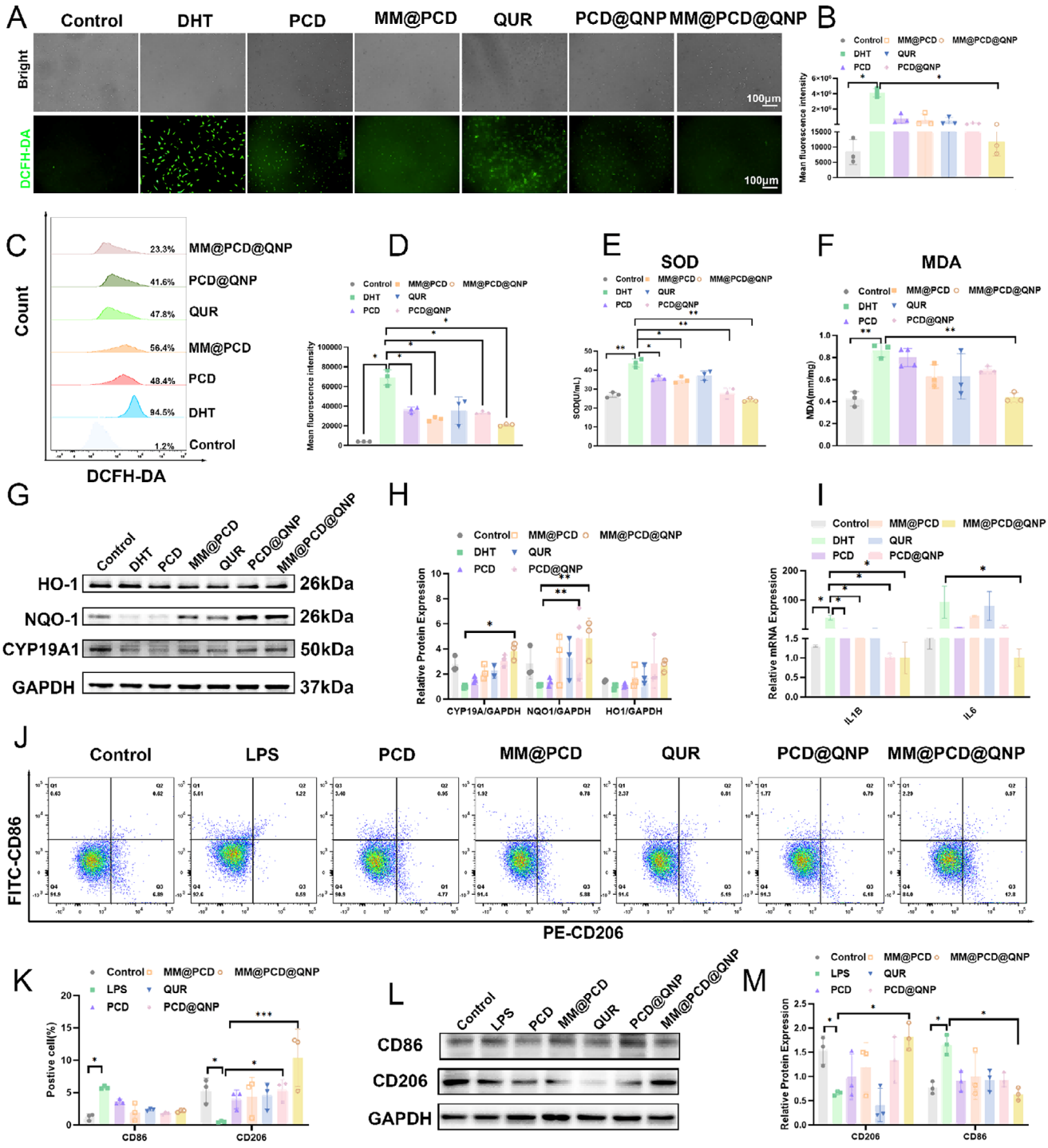

FIGURE 5 | Effects of the prepared NPs on the ROS of granulosa cells and macrophage polarization. (A) ROS staining and (B) statistics, with DCFH-DA probe brightness representing ROS levels, scale bar at 100 μM. n = 3. Nonparametric Kruskal-Wallis test with post hoc multiple comparisons. (C) Flow cytometry and statistics (D) of ROS. n = 3. Corrected Brown-Forsythe and Welch tests with post hoc multiple comparisons. (E) SOD enzyme activity and (F) MDA levels. n = 3. Corrected Brown-Forsythe and Welch tests with post hoc multiple comparisons. (G) Protein expression and (H) statistics of key antioxidant enzymes HO-1, NQO1, and estrogen synthesis key enzyme CYP19A1. n = 3. Two-way ANOVA followed by post hoc multiple comparisons. (I) mRNA expression of inflammatory factors IL-6 and IL-1B. n = 3. Corrected Brown-Forsythe and Welch tests with post hoc multiple comparisons. (J) Flow cytometry of CD86 and CD206 (macrophage polarization marker) and (K) statistics. Two-way ANOVA followed by post hoc multiple comparisons. (L) Western blot of CD86 and CD206 (macrophage polarization marker) and (M) statistics. n = 3. Corrected Brown-Forsythe and Welch tests with post hoc multiple comparisons. The data were presented as mean ± SD. *p < 0.05, **p < 0.01, ***p < 0.001.

synthesis (Figure 5G,H), indicating a potential restoration of hormonal balance.

In addition, we preliminarily evaluated the regulatory effects of our NPs on inflammation and macrophage polarization at the cellular level. Figure 5I showed that interleukin-1 beta and interleukin 6 (IL-1B and IL-6) were significantly reduced in the MM@PCD@QNPs-treated group compared to the DHT-treated KGN group (Figure 5I). Flow cytometry and western blot analysis illustrated that MM@PCD@QNPs treatment significantly reduced cluster of differentiation 86 (CD86) expression and increased cluster of differentiation 206 (CD206) expression following LPS treatment (Figure 5J–M).

2.4 | MM@PCD@QNPs Could Target Ovaries Lesions in a Hyperandrogenic Environment

A PCOS-like model was established in mice via subcutaneously injecting 6 mg/100 g of dehydroepiandrosterone (DHEA) for 21 consecutive days, followed by intraperitoneal nanoparticle administration every three days for 2 weeks. While DHEA-induced mice gained significant weight, nanoparticle treatment did not significantly alter body weight compared to controls (Figure 6A,B).

To evaluate the relative targeting of the NPs, we administered DiD-labeled NPs intraperitoneally and observed the effects in vivo (Figure S5) or ex vivo in vital abdominal organs at 1, 2, 6, 24, and 48 h after successful PCOS model establishment (n = 3). Figure S5 showed that the NPs initially accumulated within the peritoneal cavity, subsequently entering various organs through peritoneal microvessels and lymphatic vessels to exert their effects [33]. Compared to the PCD@QNPs group, MM@PCD@QNPs were cleared by the liver and spleen around 24 h later, and exhibited higher fluorescence signal intensity in the ovaries (Figure 6C). To further compare the effects of macrophage membrane encapsulation, DiD-labeled PCDs, MM@PCDs, PCD@QNPs, and MM@PCD@QNPs were intraperitoneally injected into mice for 24 h (n = 3). Ex vivo imaging revealed that the MM@PCDs and MM@PCD@QNPs groups exhibited relatively strong fluorescence signals in the ovaries (Figure 6D). Immunofluorescence co-staining for the granulosa cell marker follicle-stimulating hormone receptor (FSHR) and the DiD label revealed a stronger signal for MM@PCD@QNPs, suggesting that MM-coated NPs can be taken up more by ovarian granulosa cells than non-coated NPs (Figure 6E). These results suggested that macrophage membrane encapsulation may help improve the stability of NPs in vivo and, to some extent, alter their tissue distribution, thereby promoting their delivery to targeted organs.

2.5 | MM@PCD@QNPs Improve the Symptoms of DHEA-induced PCOS Mice by Promoting Proliferation, Inhibiting Apoptosis, and Reducing ROS Levels

For therapeutic assessment, a concentration of 5 mg/mL was selected based on a preliminary dose-ranging study (n = 3, Figure S4H–K). DHEA-induced PCOS mice exhibited classic polycystic morphology, hormonal imbalance, and disrupted estrous cycles (Figure 6K,L), while MM@PCD@QNPs treatment significantly ameliorated these pathologies: it reduced the number of cystic follicles, increased corpora lutea count, and decreased primordial follicles (Figure 6F,G). Hormonally, it lowered free testosterone (T) levels, normalized luteinizing hormone/follicle-stimulating hormone receptor (LH/FSH) ratio, and increased CYP19A1 protein expression, a key estrogen synthase, to some extent, modulating ovarian estrous cycling (Figure 6H,I). However, a notable enhancement in intraperitoneal glucose tolerance was not observed (Figure 6J). Crucially, this morphological and hormonal improvement translated to enhanced fertility. Under natural mating conditions, MM@PCD@QNPs significantly increased pregnancy rates and the number of embryos in pregnant PCOS mice (Figure 6M–O).

Consistent with in vitro findings, MM@PCD@QNPs promoted ovarian proliferation evidenced by Ki67 staining (Figure 7A,B) and suppressed apoptosis in vivo, as shown by decreased levels of apoptosis-related markers (C-CAS/CAS3 and bcl2-associated x protein/ b-cell lymphoma 2) (BAX/BCL2), along with reduced apoptosis staining intensity (Figure 7C–F). Furthermore, MM@PCD@QNPs boosted the expression of HO-1 and NQO1 (Figure 7G–J), reduced fluorescence intensity of 8-ohdg (Figure 7K,L), confirming the activation of antioxidant defenses. In addition, we found that serum antioxidant and anti-inflammatory levels were reduced in PCOS mice, and MM@PCD@QNPs could significantly increase serum SOD levels and reduce MDA, IL6 and IL-1B levels (Figure 7M–P).

2.6 | MM@PCD@QNPs May Exert Therapeutic Effects Through MAPK7/Nrf2/NQO1

To explore the potential mechanism of MM@PCD@QNPs in treating PCOS, granulosa cells from the negative control group, those treated with 500 nM DHT for 24 h, and those treated with DHT plus MM@PCD@QNPs (n = 3) were subjected to RNA transcriptome sequencing. Principal component analysis (PCA), volcano plots, and heatmaps illustrated distinct gene expression profiles among the groups (Figure 8A–D). A total of 607 differentially expressed genes (DEGs) were altered between the comparisons, with 60 overlapping genes respectively, with $P < 0.05$ and $\log_2 FC > 0.5$ (Figure 8E). Gene ontology (GO) and kyoto encyclopedia of genes and genomes (KEGG) enrichment analyses identified key pathways, including the "extrinsic apoptotic signaling pathway, " "reactive oxygen species metabolic process, " and "regulation of mitotic nuclear division" (Figure 8F,G). Among the top intersecting genes, MAPK7 (DHT_vs_NC: $\log_2 FC = -1.45$, DHT_vs_MM@PCD@QNP: $\log_2 FC = -1.30$, $P<0.05$) was significantly downregulated by DHT and restored by MM@PCD@QNP treatment (Figure 8I). Protein-protein interaction (PPI) network analysis suggested a strong functional link between mitogen-activated protein kinase 7 (MAPK7), NFE2L2 (which encodes Nrf2), and NQO1 (Figure 8H).

This led us to hypothesize that MM@PCD@QNPs act through the MAPK7-Nrf2-NQO1 axis. Western blot analysis confirmed that DHT suppressed the protein levels of phosphorylated mitogen-activated protein kinase 7 (p-MAPK7), MAPK7, Nrf2 (nuclear factor erythroid 2-related factor 2), and NQO1, which were effectively restored by MM@PCD@QNPs (Figure 9A,B).

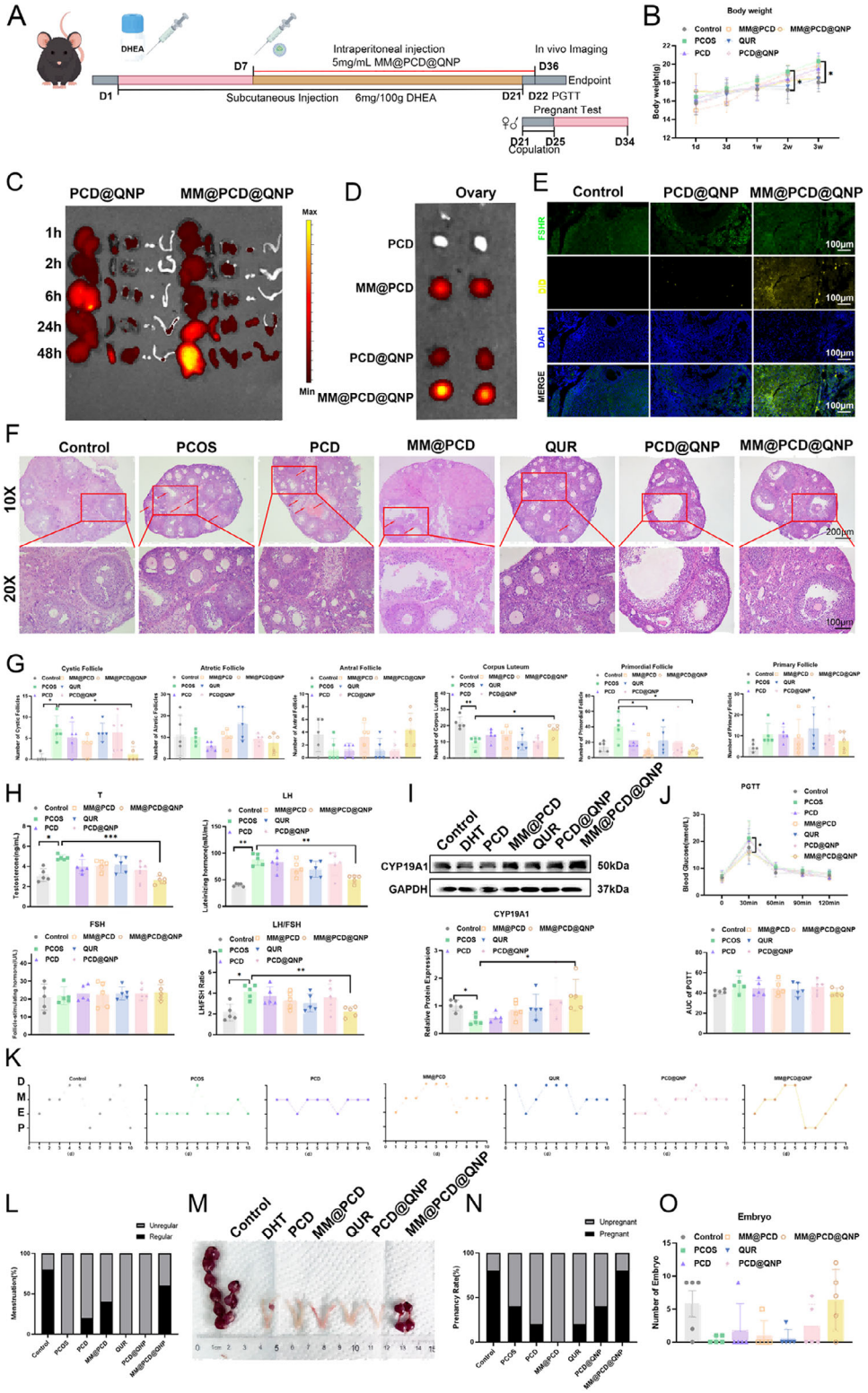

FIGURE 6 | The therapeutic effects of NPs in animals. (A) Flowchart of the animal experiment. (B) Changes in body weight of mice after DHEA modeling and NPs treatment. n = 5.Two-way ANOVA followed by post hoc multiple comparisons. (C) Ex vivo imaging (liver, spleen, kidneys, uterus, and ovaries) of DiD-labeled DNPs and MM@DNPs at 1 h, 2 h, 6 h, 24 h and 48 h after intraperitoneal injection. n = 3. (D) Representative imaging of ovaries of DiD-labeled PCD, MM@PCD, PCD@QNPs, and MM@PCD@QNPs after 24 h. (E) Fluorescence representation showing colocalization of DiD with FSHR, scale bar = 100 μM. (F) H&E staining and (G) follicle counting (antral follicles, atretic follicles, cystic follicles, corpora lutea, primordial follicles, and primary follicles) in different groups, with red boxes indicating areas of magnification, scale bars 200 and 100 μM. n = 5. Corrected Brown-Forsythe and Welch tests with post hoc multiple comparisons. (H) Hormone levels in mouse serum (testosterone, luteinizing hormone, follicle-stimulating hormone, and their ratios) measured by ELISA. n = 5. Corrected Brown-Forsythe and Welch tests with post hoc multiple comparisons. (I) Expression levels and statistics of estrogen key synthesis protein CYP19A1. n = 3. Corrected Brown-Forsythe and Welch tests with post hoc multiple comparisons.

Immunofluorescence and nuclear-cytoplasmic fractionation further demonstrated that MM@PCD@QNPs promoted the translocation of Nrf2 from the cytoplasm to the nucleus (Figure 9C–F). As MAPK7 functions upon phosphorylation, we assessed its activation state in animal models, MM@PCD@QNPs increased the phosphorylation level of MAPK7, thereby activating the entire MAPK7-Nrf2-NQO1 signaling cascade (Figure 9G,H).

To confirm the pathway's necessity, we inhibited MAPK7 phosphorylation using ERK5-IN-1 (Figure 10G,J). This inhibitor reversed the beneficial effects of MM@PCD@QNPs on proliferation, apoptosis, and ROS suppression (Figure 10A–G) in cellular models. In vivo, the inhibitor partially abrogated the therapeutic effects, leading to increasing number of atretic follicle and decreasing number of corpora lutea (Figure 10I), as well as elevating the expression of apoptotic proteins (C-CAS3/CAS3) (Figure 10J), though hormonal changes were not statistically significant (Figure 10H). This may be because ovarian hormone regulation relies on multiple cell types, and the effects of MAPK7 inhibitors were not strong enough. Western blot confirmed that MAPK7 inhibition downregulated Nrf2 and NQO1 expression in cell and animal models (Figure 10G,J). MAPK7 has been identified as a potential oncogene and prognostic marker, and its overexpression can promote the proliferation, invasion, and migration of ovarian cancer cells [34]. ROS, acting as a hub, can activate the MAPK signaling pathway and, by oxidizing cysteine residues in Keap1, trigger the release of Nrf2 from Keap1 and its translocation to the nucleus, activating the expression of antioxidant genes such as NQO1 [35], while the direct relationship between MAPK7 and ROS remains unclear. Our data preliminarily suggested that MM@PCD@QNPs ameliorated granulosa cell dysfunction and PCOS symptoms, at least in part, by activating the MAPK7-Nrf2-NQO1 signaling pathway (Figure 10K).

3 | Discussion

Based on the complexity and diversity of PCOS treatment [36, 37], this study innovatively developed a macrophage membrane-coated quercetin nano-delivery system (MM@PCD@QNPs) with low toxicity, minimal side effects, ROS-sensitive controlled drug release and relatively targeted delivery. It demonstrated that MM@PCD@QNPs effectively alleviate PCOS symptoms by activating the MAPK7-Nrf2-NQO1 pathway, promoting granulosa cell proliferation, inhibiting apoptosis, and reducing oxidative stress. This work suggests a safe, effective, and targeted treatment for PCOS and provides new insights into its molecular mechanisms, with potential for clinical application.

QUR, although promise for PCOS [10], has shown some limitations in bioavailability, stability, and targeting, restricting its clinical application [7]. Generally, the oral bioavailability of QUR is only around 10%, and its poor water solubility renders intravenous injection extremely challenging [38]. Notably, the development of functional delivery systems has been proven to significantly improve the bioavailability of QUR [39]. To date, intragastric gavage has remained main administration route of QUR in PCOS models, with doses ranging from 15 to 100 mg/kg and treatment durations ranging from 1 to 45 days [11]. The development of QUR nano-therapy for PCOS remains inadequate. Thus, designing appropriate nano-delivery systems has become a pivotal step to enhance its therapeutic potential for PCOS.

Nanoparticle drug delivery systems could overcome these challenges by promoting intracellular penetration and enhancing drug absorption [36, 37, 40]. The nano-delivery system we designed was a uniform-particle-size formulation coated with M0 macrophage cell membranes, with PCDs as the nanocore and QUR as the loaded drug. Aryl boronates, characterized by mild chemical reactivity, low toxicity, and ROS sensitivity, can be chemically coupled to DEX to form PCD nanocore. In vitro drug release experiments revealed that the presence of H_2O_2 enhanced the QUR release from PCD@QNPs, suggesting that our NPs possessed ROS-responsive properties. Different types of macrophages exert distinct functions: M0 macrophage cells primarily mediate immune evasion [41, 42], whereas M1-type ones exert anti-infective, anti-tumor and pro-inflammatory effects [43], and M2-activated ones are characterized by anti-inflammatory properties [44]. Notably, these membranes share common advantages-enhancing their circulation time and targeting efficacy [45, 46]. Our MM@PCD@QNPs preserved most M0 membrane proteins C11b and expressed SIRPα. These biomimetic NPs were less up-taken by LPS-induced macrophages and more by DHT-induced granulosa cells compared to uncoated NPs, suggesting potential for targeted delivery to lesions.

As far as we know, the preferential accumulation of MM@PCD@QNPs at the inflammatory sites and their subsequent therapeutic action require the coordination of multiple components. First, membrane-bound proteins (cluster of differentiation 47 (CD47)/ SIRPα), programmed cell death protein 1/programmed cell death protein ligand 1, and integrin family) on MM act as a "stealth shield", transmitting "don't eat me" signals to effectively evade phagocytosis by the systemic mononuclear-phagocyte system [47]. Subsequently, under inflammatory stimulation, integrins, selectins, and chemokine receptors on the MM exert synergistic effects to drive directional homing to inflamed sites [48, 49]. Cho et al. reported that high expression of ITGA2 on MM has been verified to facilitate nanoparticle migration toward ovarian cancer [50]. The ovarian microenvironment of PCOS is often accompanied by elevated ROS levels (such as $O_{\cdot 2}$ and. OH) and inflammation [34, 35, 45, 51]. Upon reaching target organs, adhesion molecules on the MM specifically interact with ligands (fibronectin, clathrin) on target cells, such as human liver cancer cells HepG2 [52], human colorectal adenocarcinoma cell (Caco-2) [53], and human neuroblastoma SH-SY5Y cells [41], thereby triggering receptor-mediated endocytosis and promoting efficient nanoparticle

(J) Glucose tolerance statistics and AUC curve in the abdominal cavity of mice. n = 5. Two-way ANOVA followed by post hoc multiple comparisons. (K) Representative images and (L) statistics of the estrous cycle of mice in different NPs treatment. (M) Pregnancy status, (N) pregnancy rates, and (O) embryo numbers of mice after mating. n = 5. Corrected Brown-Forsythe and Welch tests with post hoc multiple comparisons. The data were presented as mean ± SD. *p < 0.05, **p < 0.01, ***p < 0.001.

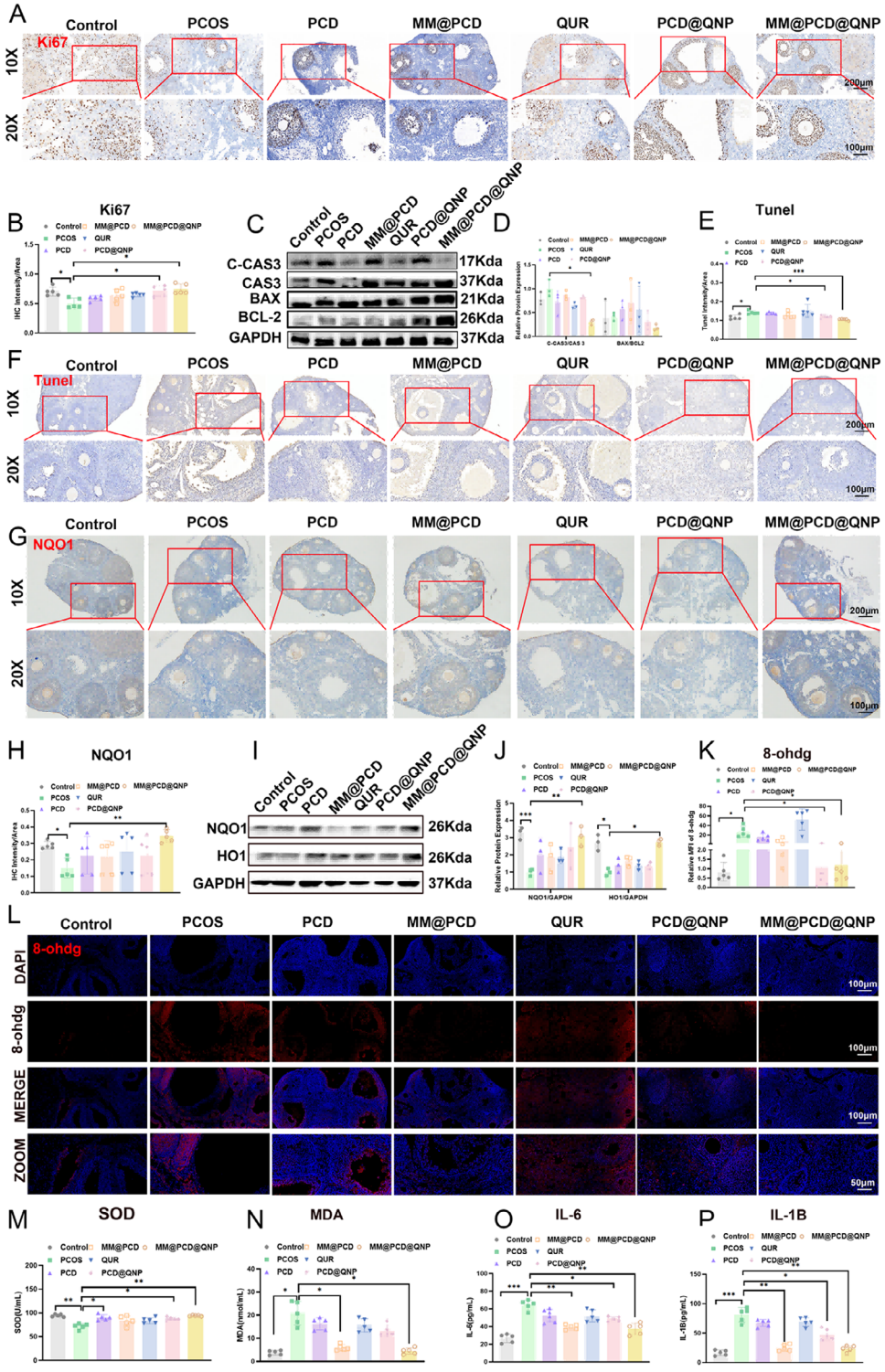

FIGURE 7 | The effects of NPs on animal functions. (A) Immunohistochemical staining and (B) statistics for the proliferation marker Ki67, scale bars are 200 and 100 μM, with red boxes indicating areas of magnification. n = 5. Corrected Brown-Forsythe and Welch tests with post hoc multiple comparisons. (C) Protein levels and (D) statistics of apoptotic markers (C-CAS3/CAS3 and BAX/BCL2) via western blot. n = 5. Two-way ANOVA followed by post hoc multiple comparisons. (E) Tunel staining and (F) statistics, scale bars are 200 and 100 μM, with red boxes indicating areas of magnification. n = 5. Corrected Brown-Forsythe and Welch tests with post hoc multiple comparisons. (G) NQO1 staining and (H) statistics, scale bars are 200 and 100 μM, with red boxes indicating areas of magnification. n = 5. Corrected Brown-Forsythe and Welch tests with post hoc multiple comparisons. (I) Protein levels and (J) statistics of antioxidant enzyme markers (NQO1 and HO1) via western blot. n = 5. Two-way ANOVA followed by post hoc multiple comparisons. (L) Immunofluorescence of 8-ohdg and (K) statistics. n = 5. Corrected Brown-Forsythe and Welch tests with post hoc multiple comparisons. (M) SOD enzyme activity and (N) MDA levels. n = 5. Corrected Brown-Forsythe and Welch tests with post hoc multiple comparisons. Levels of inflammatory factors IL-6 (O) and IL-1B (P) in mouse serum. n = 5. Corrected Brown-Forsythe and Welch tests with post hoc multiple comparisons. The data were presented as mean ± SD. *p < 0.05, **p < 0.01, ***p < 0.001.

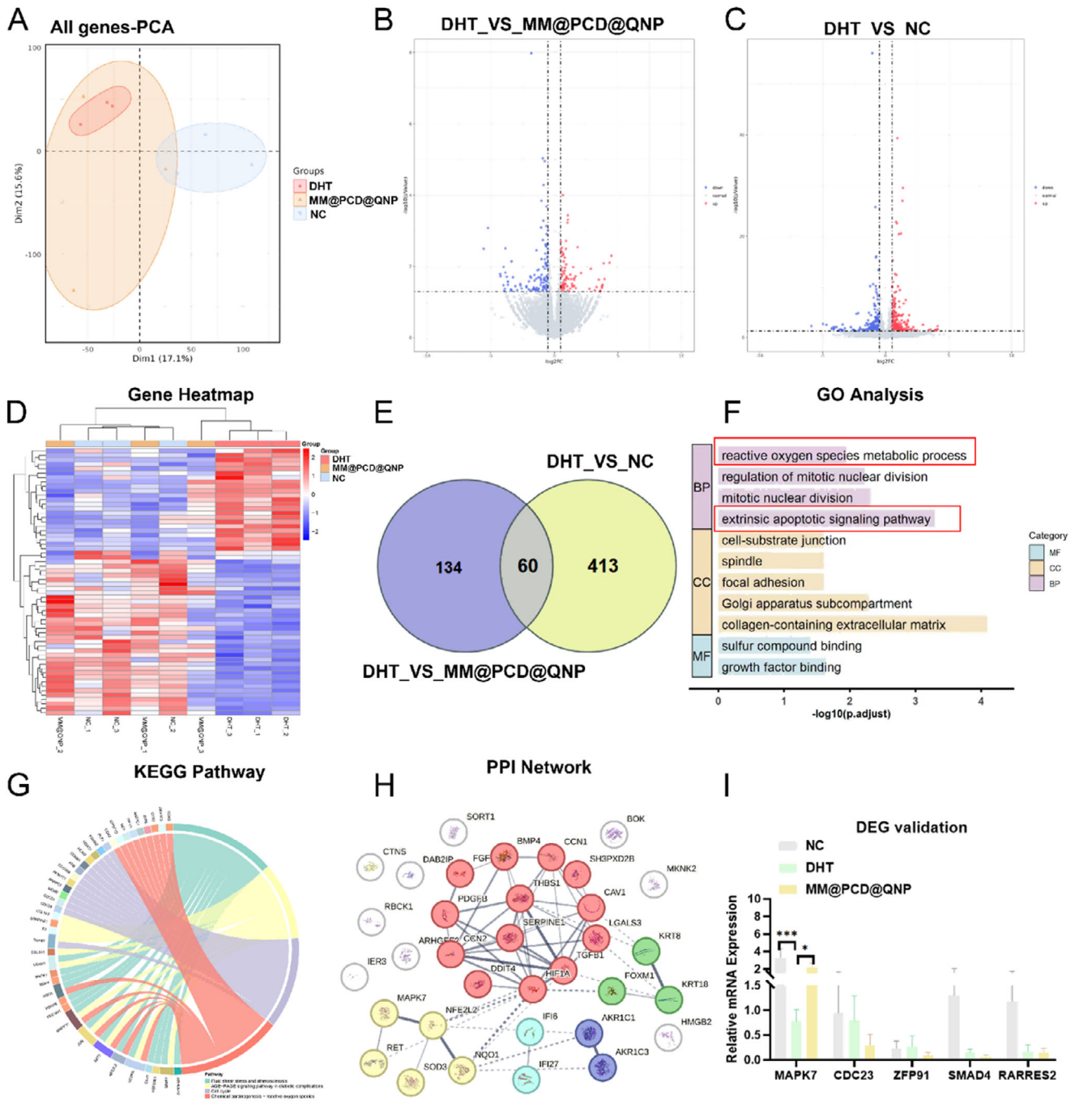

FIGURE 8 | Transcriptome sequencing and validation after NPs treatment. (A) PCA analysis of NC, DHT treatment, and DHT plus MM@PCD@QNPs treatment, as well as (B, C) volcano plots and (D) heatmaps of DEGs for NC_vs_DHT and DHT_vs_MM@PCD@QNP (N = 3). (E) Venn diagram of DEGs for NC_vs_DHT and DHT_vs_MM@PCD@QNP. (F) GO analysis and (G) KEGG analysis of all DEGs for NC_vs_DHT and DHT_vs_MM@PCD@QNP. "extrinsic apoptotic signaling pathway"and "reactive oxygen species metabolic process" were highlighted with red boxes. (H) PPI network interaction diagram focused on pathways. (I) Validation of the TOP intersecting genes for NC_vs_DHT and DHT_vs_MM@PCD@QNP by RT-qPCR. n = 5. Two-way ANOVA followed by post hoc multiple comparisons. The data were presented as mean ± SD. *$p < 0.05$, ***$p < 0.001$.

internalization [51, 54, 55]. Our in vivo and ex vivo imaging results demonstrated, that MM@PCD@QNPs were cleared by the liver more slowly, achieving targeted accumulation in ovarian inflammatory tissue, to a certain extent. Subsequently, the PCD nano-shells underwent chemical reactions with excessive ROS, leading to ester bond cleavage and thus triggering the release of QUR [56]. As a result, PCDs and QUR exert a synergistic therapeutic effect.

Impaired granulosa cell proliferation, excessive apoptosis and elevated ROS are common in PCOS [35, 57], and some free radical scavengers have been proven to alleviate PCOS symptoms by enhancing antioxidant enzymes and reducing inflammatory markers [7, 58]. Our MM@PCD@QNPs significantly mitigated granulosa cell damage and PCOS-related symptoms in mice, with a dosage far lower than conventional oral doses (100 mg/kg for 28 days) [11], showing high biocompatibility

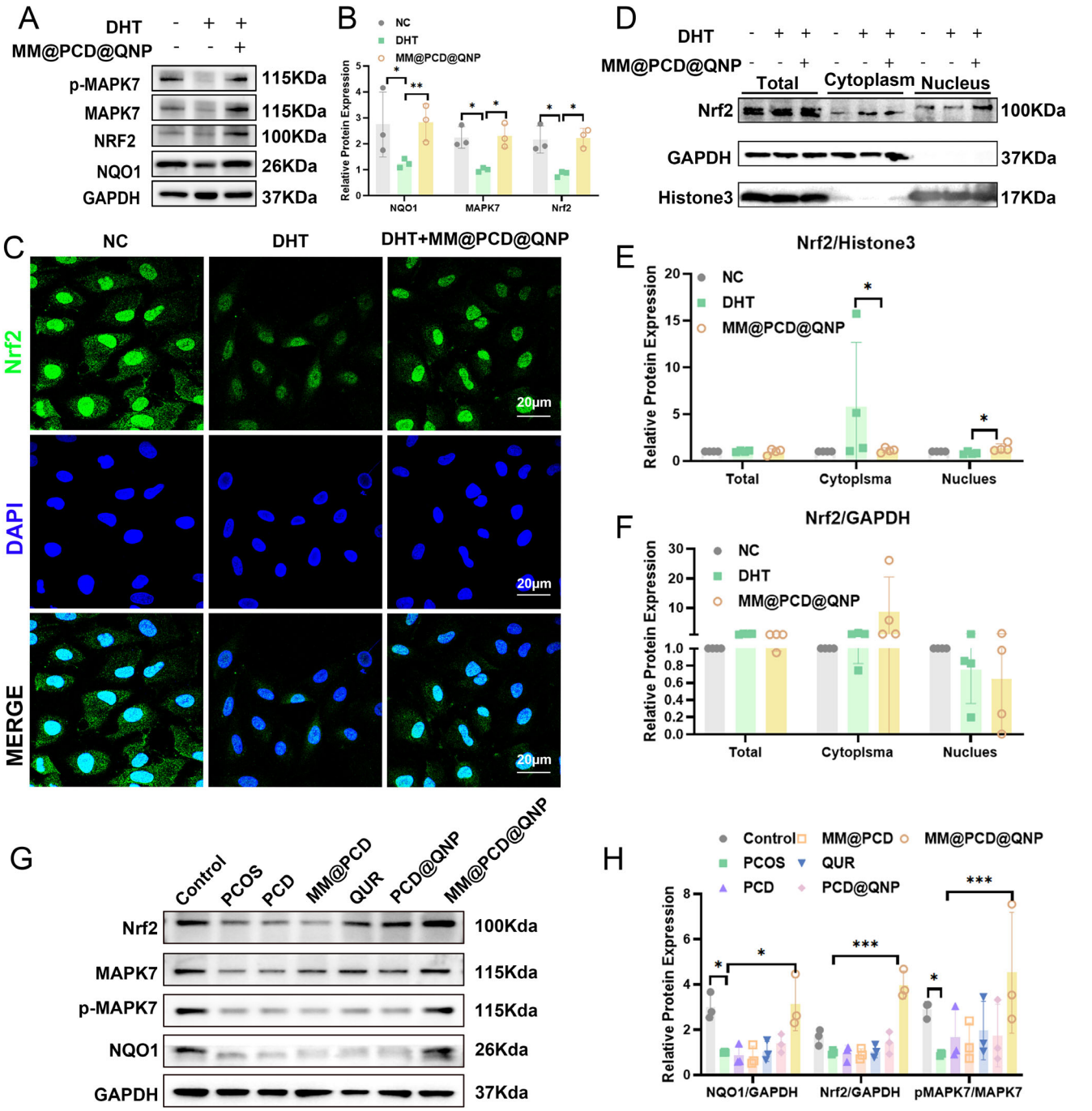

FIGURE 9 | The validation of the MAPK7-Nrf2-NQO1 signaling pathway. (A) The protein levels of MAPK7-Nrf2-NQO1 with (B) statistical analyses. (C) immunofluorescence co-localization and (D) statistics of Nrf2. Green represents Nrf2, blue represents DAPI, scale bar is 20 μM. n = 3. (E) Western bolt with (F) statistics of the nuclear-cytoplasmic protein separation of Nrf2. n = 4. (G) The protein levels and (H) statistics of the MAPK7-Nrf2-NQO1 pathway in ovarian tissue after NPs treatment. n = 3. Two-way ANOVA followed by post hoc multiple comparisons. The data were presented as mean ± SD. *$p < 0.05$, **$p < 0.01$, ***$p < 0.001$.

(low toxicity, minimal side effects). However, our PCOS model did not exhibit significant metabolic abnormalities-a finding consistent with previous studies-likely due to the absence of a high-fat diet regimen in our experimental design [34, 59, 60]. As is well established, intermittent administration can reduce the burden of drug administration and dampen the risk of immunogenicity.

Furthermore, RNA transcriptomics suggests that the MAPK7-Nrf2-NQO1 signaling pathway may explain the potential therapeutic mechanism of MM@PCD@QNPs. MAPK7 (also known as ERK5), a downstream molecule in the MAPK family, plays a key role in cell proliferation, differentiation, and survival [61]. Previous literature has shown that the MAPK/ERK signaling pathway is closely associated with cell proliferation, apoptosis,

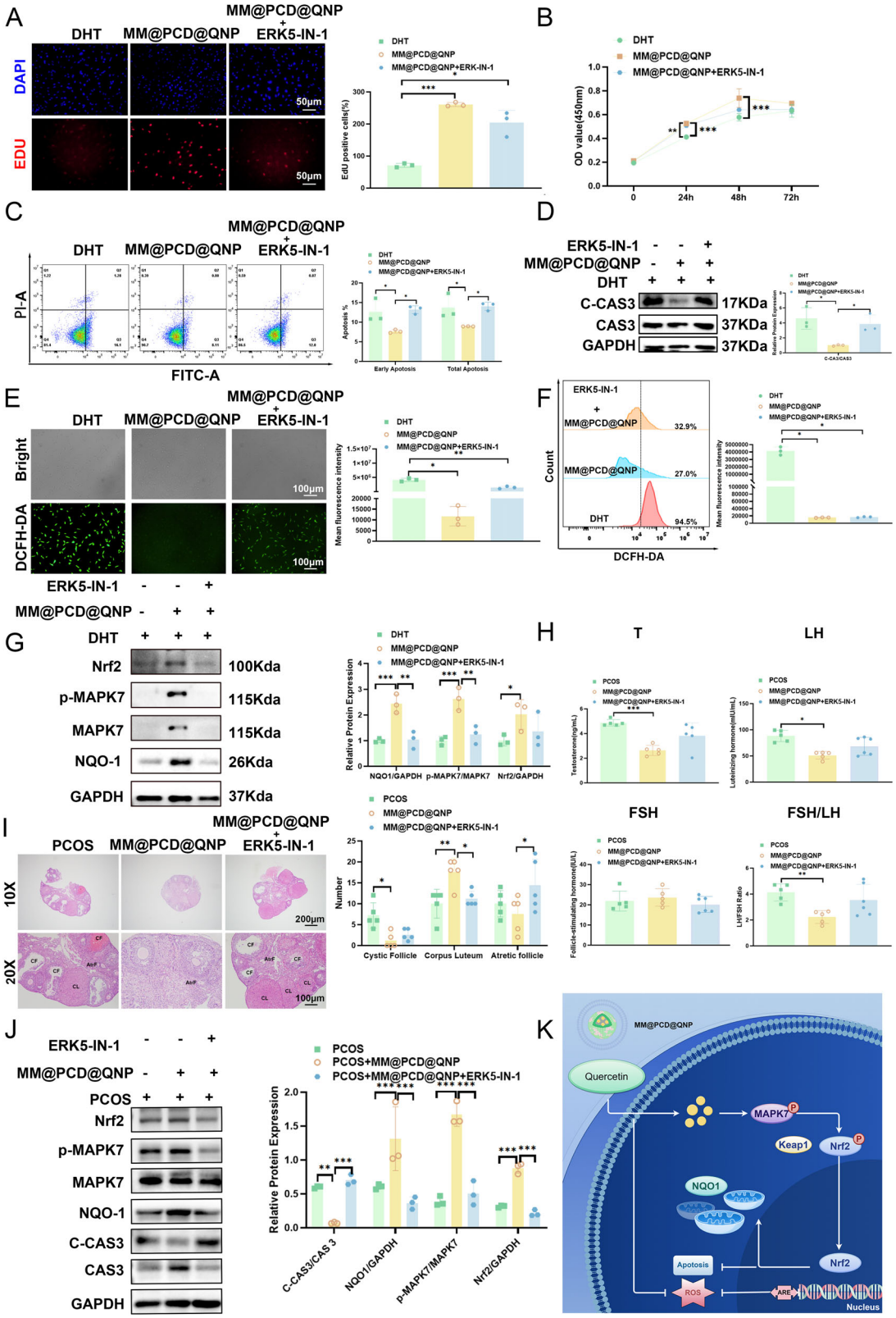

FIGURE 10 | MM@PCD@QNPs may affect granulosa cell and ovarian function through the MAPK7-Nrf2-NQO1 pathway. After DHT, MM@PCD@QNPs, and ERK5-IN-1 (MAPK7 inhibitor) treatment, (A) Edu staining and statistics, with red representing proliferative cells and blue representing DAPI, scale bar at 50 μM. n = 3. Corrected Brown-Forsythe and Welch tests with post hoc multiple comparisons. (B) CCK8 analysis, plotted using OD values. n = 3. Two-way ANOVA followed by post hoc multiple comparisons. (C) Flow cytometry visualization and statistics of KGN apoptosis; the x-axis represents the FITC channel, the y-axis represents the PI channel, FITC positive and PI negative indicate early apoptotic cells, FITC and PI double positive indicate necrotic cells, the sum of both indicates total apoptotic cells. n = 3. Two-way ANOVA followed by post hoc multiple comparisons. (D) Key apoptotic proteins (C-CAS3/CAS3) and statistical analyses. n = 3. Corrected Brown-Forsythe and Welch tests with post hoc multiple comparisons.

and ROS levels in many diseases [62–64]. However, few studies have focused on the mechanisms involved in MAPK7. Nrf2 is a crucial transcription factor for the anti-oxidative stress response, which separates from Keap1, moves to the nucleus, and antioxidant response element (AREs) to regulate enzymes like NQO1, protecting cells from oxidative damage [65]. This study found that DHT treatment reduced MAPK7, Nrf2, and NQO1 expression in PCOS cells and mice, but MM@PCD@QNPs treatment restored these levels, suggesting it may alleviate PCOS symptoms via the MAPK7-Nrf2-NQO1 pathway. While MAPK7 inhibitor improved granulosa cell function, they did not significantly affect hormone production, possibly due to the far greater complexity of animal models than in vitro cell models, and in vitro results may not fully reflect the complex physiological and pathological processes in vivo [66]. In summary, these results suggest a promising initial advance in the mechanism of effective QUR delivery by MM@PCD@QNPs for PCOS.

This study has achieved several innovative breakthroughs in the treatment of PCOS. First, to address the objective limitations of QUR, this study designed and synthesized a novel, low-toxicity, low-side-effect, and highly biosafe ROS-sensitive macrophage membrane-coated nano-delivery system. Second, we experimentally screened the optimal dosage of MM@PCD@QNPs, providing a certain reference for the clinical transformation of our nano-drug delivery systems. More importantly, this study innovatively proposed that the MAPK7-Nrf2-NQO1 signaling pathway may be a key pathway in the pathogenesis and treatment of PCOS, highlighting its potential role in cell proliferation, apoptosis, and ROS regulation. Furthermore, the supplemented fertility studies enrich the research landscape of PCOS therapeutics. These findings not only provide new insights and potential targets for PCOS treatment but also lay the foundation for future PCOS nano-drug development.

However, there are some limitations to that need to be discussed. For example, only intraperitoneal injection was used to conduct experiments on the mouse PCOS model and did not directly compare it with the commonly used intravenous injection in clinical practice. Only cellular-level transcriptome sequencing was done, missing animal tissue insights. The therapeutic mechanism via the MAPK7-Nrf2-NQO1 pathway is not fully explored. Macrophage membranes derived from the laboratory are affected by factors such as cell culture conditions and extraction processes, making it difficult to ensure that each batch of cell membranes is completely consistent in protein composition and content, resulting in some batch effects. There is a lack of exploration on long-term reproductive safety. Our future work will focus on comparison of administration methods, establishing a standardized identification and extraction process for macrophage membrane proteins, more in-depth mechanistic research and reproductive safety evaluation to enhance understanding and clinical application.

4 | Conclusion

This study developed a novel, low-toxicity macrophage membrane-coated biomimetic QUR nano-delivery system with stable nanoscale size, ROS sensitivity, and targeted, sustained release. The MM@PCD@QNPs effectively improved PCOS symptoms by activating the MAPK7-Nrf2-NQO1 pathway, promoting granulosa cell growth, reducing apoptosis, and lowering ROS levels. This approach offers a safe, targeted treatment for PCOS and introduces the MAPK7-Nrf2-NQO1 pathway as a new mechanism for understanding and treating the disease.

5 | Methods

5.1 | Materials and Reagents

Quercetin was purchased from MedChemExpress (New Jersey, USA), N,N′-carbonyldiimidazole (CDI), 4-dimethylaminopyridine (DMAP), and formamide were purchased from Shanghai McLean Biochemical Co., Ltd. (Shanghai, China); 4-(hydroxymethyl)phenylboronic acid pinol ester and dextran (molecular weight:3500) were purchased from Shanghai Aladdin Biochemical Technology Co., Ltd. Methanol, dichloromethane, anhydrous magnesium sulfate, hydrogen peroxide (H_2O_2), dimethyl sulfoxide, deuterated dimethyl sulfoxide (DMSO-d_6), and deuterated methanol (methanol-d_4) were purchased from Sinopharm Chemical Reagent Co., Ltd. Flasks, dialysis clips and dialysis bags (3500 kilodalton), magnetic rotors were purchased from Shanghai Yuanye Bio-Technology Co., Ltd. Cell membrane extraction kits were purchased from Beyotime Biotechnology Research Institute Co., Ltd. 1, 19-Dioctadecyl-3, 3, 39, 39-tetramethyl-1, 3-dicarboxycyanine perchlorate was purchased from Biotium Inc (Fremont, USA).

5.2 | Extraction of Macrophage Membranes

Raw 264.7 cells (ATCC, USA) were cultured to confluence in DMEM supplemented with 10% fetal bovine serum and 1% penicillin-streptomycin at 37°C in a 5% CO_2 atmosphere. Cells were counted using a counting chamber and 10^{*7} cells/dish were harvested for subsequent membrane extraction. Following the manufacturer's instructions, cells were washed with pre-chilled PBS (Servicebio, 0.01 M, pH 7.4) and lysed on ice for 15 min using Membrane Protein Extraction Reagent A containing 1% phenyl-

(E) ROS staining and statistics, with DCFH-DA probe brightness representing ROS levels. n = 3. Corrected Brown-Forsythe and Welch tests with post hoc multiple comparisons. (F) Flow cytometry and statistics of ROS. n = 3. One-way ANOVA followed by post hoc multiple comparisons. (G) The cell protein expression of MAPK-Nrf2-NQO1 pathway and quantification via western blot. (H) Hormone levels in mouse serum (testosterone, luteinizing hormone, follicle-stimulating hormone, and their ratios) measured by ELISA. n = 5. Corrected Brown-Forsythe and Welch tests with post hoc multiple comparisons. (I) H&E staining and follicle counting after NP treatment, with scale bars 200 and 100 μM, n = 5. Two-way ANOVA followed by post hoc multiple comparisons. AtrF, CF and CL represent atretic follicles, cystic follicles and corpora lutea, respectively. (J) The animal protein expression of MAPK-Nrf2-NQO1 pathway and C-CAS3/CAS3 and quantification via western blot. n = 3. Two-way ANOVA followed by post hoc multiple comparisons. (K) Schematic diagram of the potential mechanism. The data were presented as mean ± SD.*$p < 0.05$, **$p < 0.01$, ***$p < 0.001$.

methanesulfonyl fluoride, and then triturated 50 times with a glass homogenizer. After ensuring sufficient cell disruption, the cell suspension was centrifuged at 3000 rpm at 4°C for 20 min to keep the supernatant and centrifuged at 13000 rpm at 4°C for 30 min to collect the cell pellet. After adding Membrane Protein Extraction Reagent B, the membrane protein solution was purified by brief vortexing and centrifuging at 14 000 rpm on ice for 5 min for three times and stored at −80°C. Protein concentration and quality were determined using the BCA assay (Elabscience, China).

5.3 | MM@PCD@QNP Synthesis

Dissolve 1947 mg of CDI and 1404 mg of PBAP in 20 mL of dichloromethane in a 25 mL dry round-bottom flask and stir at room temperature for 1 h. The collected organic phase was further washed with saturated saline for three times, dried over anhydrous magnesium sulfate, and then subjected to rotary evaporation in a vacuum dryer for 2 h to obtain activated CDI-PBAP. Then, dissolve 226.8 mg of DMAP, 135 mg of DEX, and 540 mg of CDI-PBAP in 15 mL of DMSO and stir magnetically at 37°C for 24 h to obtain the PABP conjugated with DEX polymer, which was further placed in an activated dialysis bag (MWCO of 3500 Da) and dialyzed against double-distilled water(overnight), and collected and centrifuged at 12, 000 rpm for 15 min to drying using a freeze dryer (Millrock Technology, USA). Different ratios of PCD and QUR were dissolved in formamide and methanol (1:1, v/v), and then added dropwise to double-distilled water under magnetic stirring, and finally dialyzed using a 3500 Da dialysis bag to remove unloaded drug and organic reagents, obtaining membrane-free PCD@QNPs. M0 macrophage membranes and the PCD@QNPs solution were sonicated on ice for 15 min at a mass ratio of 1:1, and then then repeatedly extruded through a liposome extruder (Avanti-610000, Merck, USA) containing a 200 nM filter to obtain a uniform MM@PCD@QNPs. The synthesis steps and exploration process were shown in Figures S2 and S3.

5.4 | Cell Culture and Treatment

Primary mouse ovarian granulosa cells (CP-M050, Procell, China), KGN, THP-1, and Raw 264.7 cells were cultured in DMEM/F12, 1640, and DMEM supplemented with 10% fetal bovine serum and 1% penicillin/streptomycin, respectively, at 37°C in a 5% CO_2 incubator. KGN cells were treated with 500 nM DHT (m6033, Abmole, China) for 24 h, and macrophages were treated with 100 ng/mL phorbol 12-myristate 13-acetate (PMA), followed by 100 ng/mL LPS (L8880, Merck, USA) for 24 h.

5.5 | Animal Modeling

All animal experiments were conducted in compliance with the Experimental Animal Ethics Committee of Wuhan University (approval number: 20240402B). A total of 91 female C57BL/6 mice (3 weeks old) and 18 male C57BL/6 mice (8 weeks old) were obtained from Jiangsu Jicui Pharmaceutical Biotechnology Co., Ltd. The animals were housed at 20 ± 5°C, 43–47% relative humidity, and a 12-h light-dark cycle, with a standard laboratory diet and water provided. Mice were housed for 3 days prior to the experiment to acclimate to the conditions.

DHEA was dissolved in olive oil and ethanol (50:1) and injected subcutaneously for 21 consecutive days at a dose of 6 mg/100 g body weight to create PCOS mice as previous reported [14]. Control group received the same dose of olive oil injected subcutaneously. The animal experiments were divided into the following 7 groups: Control (olive oil via subcutaneous + normal saline via i.p), PCOS (PCOS modeling + normal saline via i.p), PCD (PCOS modeling + 15 mg/kg weight PCDs via i.p), MM@PCD (PCOS modeling + 15 mg/kg weight MM@PCDs via i.p), QUR (PCOS modeling +15 mg/kg weight QUR via i.p), PCD@QNP (PCOS modeling + 15 mg/kg weight PCD@QNPs via i.p), MM@PCD@QNP (PCOS modeling + 15 mg/kg weight MM@PCD@QNPs via i.p), ERK5-IN-1 (PCOS modeling + 15 mg/kg weight MM@PCD@QNPs via i.p + 1 mg/kg body weight ERK5 inhibitor via i.p). All animals were divided into three batches for evaluation of treatment efficacy, fertility, and drug distribution. Reference to previous studies [67], treatment was administered every three days for two weeks, and mice were sacrificed under isoflurane anesthesia. Blood samples were collected from the eyes, centrifuged, and stored at −80°C for biochemical analysis and ELISA.

5.6 | Nanoparticle Characterization

The chemical structures of PCDs and PCD@QNPs, as well as QUR, were characterized by 400 MHz ^{1}H nuclear magnetic resonance (^{1}H-NMR) spectroscopy on a Bruker Avance AVII-400 spectrometer (Bruker Corporation, Karlsruhe, Germany), for the purpose of analyzing hydrogen bonding interactions. Specifically, PCDs and PCD@QNPs were dissolved in a mixed solvent of DMSO-d_6 and CD_6OD (methanol-d_4, 1:1, v/v), whereas QUR was solubilized in pure DMSO-d_6 for spectral acquisition. The size and zeta potential of the NPs were measured using dynamic light scattering using a Malvern Zetasizer Nano ZS (Nano ZS 90, Malvern, UK). A drop of 10 μg/ml nanoparticle solution was deposited on a copper grid, dried, and negatively stained with 1% uranyl acetate [49]. The morphology and size of PCD@QNPs and MM@PCD@QNPs were determined using a TEM (LIBRA 200 FE, Zeiss, Germany) at 200 kV. FTIR (NICOLET 5700, Thermo Fisher Scientific, USA) was used to obtain infrared absorption spectra of the samples and identify key functional groups and chemical bonds. For the stability assay, 1 mL of a 10 μg/mL nanoparticle solution was mixed with 9 mL of 10 mM PBS (pH = 7.4) to monitor size and zeta potentials of the NPs over a period of three weeks.

5.7 | Drug Loading and In Vitro Release Experiments

The optical density (OD) values were recorded at 374 nm using a UV–vis spectrophotometer (DU730, Beckman Coulter). Drug loading efficiency (DLE) and drug encapsulation efficiency (DEE) were measured based on a drug concentration standard curve and the following equations.

$$\text{DLE} = \text{Mass of QUR} / (\text{Mass of PCD} + \text{Mass of QUR})$$

$$DEE = \text{Mass of QUR} / (\text{Mass of added QUR})$$

PCD@QNPs and MM@PCD@QNPs were dialyzed against 10 mL of solvent (PBS: DMSO = 8:2, v/v) with or without 500 nm H_2O_2 solution [68]. The volume of drug released was measured by recovering 1 mL of solvent at a fixed time (0, 30 min, 2 h, 8 h, 16 h, 1 d, 3 d, 5 d, 7 d), which was then topped up with 1 mL of fresh solvent. The cumulative drug release rate was calculated according to the following equation, and drug release curves were plotted.

$$\text{Cumulative drug release} = M_t / M_0 \text{x } 100\%$$

where M_t and M_0 represent the amount of drug released at time t and the initial amount of drug in the NPs, respectively.

5.8 | DiD-labeled NPs Synthesis and In Vitro Uptake

PCDs, QUR, and DiD were dissolved in a formamide/methanol mixture (1:1, v/v) at a mass ratio of 7:2:1 and added dropwise into double-distilled water under magnetic stirring, followed by dialyzing (MWCO 3500 Da) to remove free drugs and organic solvents, ultimately yielding DiD-labeled NPs. These NPs were subsequently mixed with macrophage membranes at a 1:1 mass ratio, sonicated in an ice bath, and repeatedly extruded using a liposome extruder to obtain DiD-labeled NPs coated with macrophage membranes. Raw264.7 and THP-1 cells were incubated with 10 μg/mL DiD-labeled PCD@QNPs and MM@PCD@QNPs for 4 h, while primary mouse ovarian granulosa cells and KGN cells were cultured with the same formulations for 24 h, and then visualized under a confocal microscope (FV1200, Olympus, Japan), with three random fields of view used for analysis.

5.9 | Transcriptome Sequencing (RNA-Seq) and Bioinformatics Analysis

Following the reagent manufacturer's instructions (APExBIO, USA), the total RNA of NC, DHT and DHT+MM@PCD@QNP treatments (n = 3) for 24 h was extracted to construct libraries, and high-throughput sequencing was performed to obtain raw gene expression data. Bioinformatics analysis was used to identify differentially expressed genes, including GO enrichment analysis, KEGG pathway analysis and Protein-Protein Interaction Networks (PPI) networks.

5.10 | Network Pharmacology

The ChEMBL (https://www.ebi.ac.uk/chembl/) and SwissTargetPrediction databases (http://swisstargetprediction.ch/) were used to obtain the common predicted targets of quercetin, and the GeneCards database was used to obtain the predicted targets of PCOS. The intersection of the two predicted targets was used to draw a Venn diagram, and then Gene Ontology (GO) enrichment analysis, Kyoto Encyclopedia of Genes and Genomes (KEGG) pathway analysis were performed.

5.11 | ROS Scavenging Detection

The DCFH-DA probe was incubated with KGN cells at a dilution ratio of 1:1000 for 1 h. Intracellular ROS levels were recorded using the 488 channel of fluorescence microscopy and FITC channel of a flow cytometer. Following the protocol in the reagent manual, intracellular SOD enzyme activity (A001-3-2, NanJing JianCheng Bioengineering Institute, China) and MDA (A003-4-1, NanJing JianCheng Bioengineering Institute, China) were measured using a microplate reader (Perkinelmer, Massachusetts, USA), reflecting the nanomaterial's ability to scavenge ROS.

5.12 | Hemolysis Analysis

Fresh red blood cells from healthy mice were washed three times with PBS by centrifugation at 3000 rpm for 5 min to prepare a 4% red blood cell solution. 1 mL of nanomaterial sample of different concentrations and groups was added to 1 mL of a 4% red blood cell pellet and incubated at 37°C for 3 h, and then centrifuged at 3000 rpm for 10 min to observe whether hemolysis occurred. 100 μL of the supernatant was sampled and transferred to a 96-well plate to measure the absorbance at 577 nm (Perkinelmer, Massachusetts, USA) to quantify the degree of hemolysis. Double distilled water (positive control, complete hemolysis) and normal saline (negative control, no hemolysis) were set up for control to record OD values. Hemolysis rate (%) = (sample—negative control) / (positive control—negative control).

5.13 | Proliferation and Viability Assay

Cell Counting Kit-8 (E-CK-A362, Elabscience, China) was used to monitor cell proliferation. KGN cells were seeded in 96-well plates (100 μl, 3, 000 cells/well). After cell attachment, DHT and different NPs were treated for 24, 48, or 72 h. At each of these time periods, 10% CCK-8 reagent was added and incubated at 37°C for 1 h. The OD values at 450 nm was measured using a microplate reader. Following the manufacturer's instructions, 10 μM Edu reagent (E-CK-A377, Elabscience, China) was co-incubated with the cells for 2 h. Following fixation, permeabilization, fluorescent labeling, and DNA labeling, cell proliferation was observed under a fluorescence microscope at a wavelength of 594 nm. 200 μL of Calcein AM/PI working solution (E-CK-A354, Elabscience, China) was incubated with the cells at 37 °C for 30 min. The percentages of live and dead cells were observed under a fluorescence microscope at 488 nm (green fluorescence, live cells, Calcein) and 594 nm (red fluorescence, dead cells, PI), respectively.

5.14 | Apoptosis Detection

Flow cytometry was used to detect cell apoptosis using an Annexin V-FITC/PI detection kit (E-CK-A211, Elabscience, China) according to the manufacturer's instructions. Calibrate compensation for FITC/PI apoptosis flow cytometry by acquiring single-stained FITC+ and PI+ cell samples to eliminate spectral overlap between the two fluorescence channels. Early apoptotic cells were FITC-positive and PI-negative, while late apoptotic cells were both FITC- and PI-positive. And then, ovarian tissue

slices are dehydrated, permeabilized, and co-incubated with tunel reaction solution (E-CK-A320, Elabscience, China), followed by DAB (3, 3′-diaminobenzidine) staining and nuclear counterstaining. Finally, after dehydration and mounting, apoptotic cells are observed under a microscope. Fix cells and perform JC-1 staining and imaging (C2003S, Beyotime, China) according to the instructions, where red represents aggregates and green represents monomers.

5.15 | Immunofluorescence

Cells were seeded onto coverslips or culture dishes or tissue sections were prepared to stain 8-hodg (GB150115, Servicebio, China), Nrf2 (T55136, Abmart, China) and FSHR (ab113421, Abcam, USA). After fixation and permeabilization with 0.3% Triton-X, cells were blocked with 5% bovine serum albumin (BSA) for 1 h, incubated with primary antibodies (overnight at 4°C), washed, and incubated with fluorescently labeled secondary antibodies (such as Alexa Fluor 488 or Alexa Fluor 594-labeled antibodies) at room temperature for 1 h in the dark. Finally, cell nuclei were counterstained with DAPI or Hoechst and imaged using a confocal laser scanning microscope (CLSM) or fluorescence microscope.

5.16 | Western Blot

A certain amount of tissue and cellular proteins were separated by SDS-PAGE and transferred to a polyvinylidene fluoride membrane (Millipore, USA). After blocking, the membrane was incubated with primary and secondary antibodies and finally visualized by chemiluminescence (BioRad, USA). The antibodies used were as follows: GAPDH (10494-1-AP, Proteintech, USA), BAX (AF0120, Affinity, China), BCL-2 (T40056, Abmart, China), CAS3 (caspase-3) (AF6311, Affinity, China), C-CAS3 (cleave-caspase-3) (GB11532, Servicebio, China), HO1 (43966, Cell Signal Technology, USA), NQO1 ((NAD(P)H quinone oxidoreductase 1)) (DF6437, Affinity, China), CYP19A1(16554-1-AP, Proteintech, USA), MAPK7 (DF6835, Affinity, China), phospho-MAPK7 (TA8146, Abmart, China), Nrf2 (T55136, Abmart, China), CD206 (18704-1-AP, Proteintech, USA), CD86 (ab220188, Abcam, USA).

5.17 | Real-time Quantitative Polymerase Chain Reaction (RT-qPCR)

Total RNA was extracted from cells or tissues and cDNA was synthesized using a reverse transcription kit (Vazyme, China). Subsequently, real-time quantitative PCR was performed using SYBR Green reagent (Vazyme, China) and normalized using housekeeping genes such as ACTB as internal controls to calculate the relative expression of the target gene. The primer sequences used were listed in Table S1.

5.18 | Immunohistochemical Staining

5uM tissue sections were dewaxed, antigen retrieved, blocked, and then incubated according to the primary and secondary antibody incubation steps. Finally, they were developed with DAB and counterstained with hematoxylin. The results were observed under a microscope, and 3 fields of view were randomly selected for statistical analysis. The antibodies used and their dilution ratios were as follows: Ki-67 (GB121141, Servicebio, 1:300), NQO1 (1:100) and HO1 (10701-1-AP, Proteintech, 1:200).

5.19 | Enzyme-linked Immunosorbent Assay (ELISA)

ELISA kits for mouse IL-1B, IL-6, T, LH, and FSH were purchased from Shanghai Hualianke Biotechnology Co., Ltd. The kits were operated according to the manufacturer's instructions. Color changes were generated by enzymatic reactions, and absorbance values were read at specific wavelengths (usually 450 nm or 650 nm).

5.20 | Analysis of Liver and Kidney Function

Biochemical indicators were purchased from Nanjing Jiancheng Bioengineering Institute. ALT (C009-2-1) and AST (C010-2-1) were used to evaluate liver function, BUN (C013 - 2 - 1) and CRE (C011 - 2 - 1) were used to evaluate kidney function. TG (A110-1-1), TC (A111-1-1), HDL (A112-1-1) and LDL (A113-1-1) were used to assess obesity in mice.

5.21 | Estrous Cycle Staining and Fertility Analysis

Vaginal secretions from mice were collected using a clean cotton swab and placed on a slide at 8:00-9:00 AM daily, which lasted 10 days, covering approximately 2 estrus cycles. After fixing with 95% ethanol for 10 min, washing, staining with hematoxylin for 5 min, washing, and staining with eosin for 3 min, the samples were allowed to dry and then observed under a microscope. The estrous cycle stage was determined based on cell morphology, size, presence of nuclei, and the ratio of leukocytes to keratinocytes [67]. Based on previous literature, female and male mice were co-housed at a 2:1 ratio for one estrous cycle and then separated [69]. Nine days later, the female mice were observed for pregnancy and the number of embryos.

5.22 | H&E Staining and Follicle Counting

Following fixation in 4% paraformaldehyde, heart, liver, spleen, lung, kidney, uterus and ovarian tissues were embedded in paraffin, sectioned at 5 μm, and stained with H&E. Follicles were counted in every tenth section and categorized based on distinct morphological features into primordial, primary, and atretic and luteal stages, as previously described [67].

5.23 | Intraperitoneal Glucose Tolerance Test

After fasting mice overnight, a 20% glucose solution was injected intraperitoneally. Blood samples were collected from the tail tip at different time points including 0, 30, 60, 90, and 120 min to

test blood glucose levels using a glucometer. A blood glucose-time curve was plotted and the area under the curve (AUC) was calculated to assess glucose tolerance [14].

5.24 | In Vivo and Isolated Organ Imaging

Mice were injected with DiD fluorescently labeled NPs at a dose of 15 mg/kg body weight, and in vivo and ex vivo imaging was performed at 1 h, 2 h, 6 h, 24 h, and 48 h. Fasting for 16 h, mice in different groups were anesthetized with gas or their organs were isolated and placed in a small animal 3D in vivo optical imaging system (IVIS Lumina III, PerkinElmer, USA) to capture the fluorescence signals, and normalized analysis was performed to quantify the fluorescence intensity.

5.25 | Flow Cytometry of Macrophage Polarization

PMA-induced M0 cells were pre-treated with LPS (100 ng/mL) for 24 h, then with normal medium, LPS, PCDs, MM@PCDs, QUR, PCD@QNPs or MM@PCD@QNPs for an additional 24 h. Cells were harvested, resuspended in staining buffer containing 1% BSA, and blocked for 30 min on ice in the dark to abrogate non-specific binding, followed by staining with FITC-conjugated anti-mouse CD86 antibody (1:100) for 45 min under the same conditions. After fixation and permeabilization with a commercial fixative-permeabilization buffer, cells were stained with PE-conjugated anti-mouse CD206 antibody (1:100) for another 45 min under the aforementioned conditions. FITC and PE single-stain tubes were prepared in parallel for channel compensation to eliminate fluorescence spillover. Following three washes with cold staining buffer, cells were resuspended in 300 μL of the buffer and analyzed by flow cytometry to determine CD86 and CD206 expression levels.

5.26 | Statistical Analysis

All statistical analyses followed standardized procedures. The data were presented as mean ± SD. For numerical variables, normality was tested before using standard ANOVA, Corrected Brown-Forsythe and Welch tests with post hoc multiple comparisons, or nonparametric Kruskal-Walli's test with post hoc test. For categorical variables, the chi-square test was used. All statistical graphs were generated using GraphPad Prism 8.0, OriginLab 2019b, and R (4.5.1). The abstract scheme and flowcharts were beautified using Figdraw (2.0). $P < 0.05$ was considered significant and was marked with *, $P < 0.01$ with **, and $P < 0.001$ with ***.

Author Contributions

W.Z.L. performed conceptualization (lead), data curation (lead), formal analysis (lead), investigation (lead), methodology (lead), visualization (lead), wrote-original draft, wrote-review, and edited; Y.G. performed investigation (supporting), wrote-original draft (supporting), wrote-review, and edited (supporting); N.S. performed investigation (supporting), methodology (supporting), visualization (supporting); Z.M.D. performed data curation (supporting), visualization (supporting). F.Z. performed investigation (supporting), wrote-review, and edited; T.L.Y. performed investigation (supporting), funding acquisition (supporting), resources (co-lead); Y.B.Y performed resources (co-lead), investigation (supporting), methodology (supporting); J.C. performed conceptualization (co-lead), wrote-review, and edited (supporting); W.Y.J. performed conceptualization (co-lead), methodology (supporting), wrote-review, and edited (supporting); Z.N.Y. performed conceptualization (lead), supervision (lead), wrote-review and editing (lead).

Acknowledgements

This study would like to thank the Central Laboratory of Wuhan University Renmin Hospital for providing the experimental platform and careful guidance. This study was supported by the grants from National Natural Science Foundation of China (Grant No.82571895, Grant No. 82271672), the Shenzhen Science and Technology Program (Grant No. JCYJ20240813111408012, Grant No. JCYJ20220530140609020).

Open access publication funding provided by FCT (b-on).

Ethic Statement

All animal experiments were conducted in compliance with the Experimental Animal Ethics Committee of Wuhan University (approval number: 20240402B).

Conflicts of Interest

The authors declare no conflicts of interest.

Data Availability Statement

The databases used for network pharmacology are public and can be accessed publicly at https://www.ebi.ac.uk/chembl/, http://swisstargetprediction.ch/ and https://www.genecards.org/. The other data that support the findings of this study are available from the corresponding author upon reasonable request.

References

1. N. Helvaci and B. O. Yildiz, "Polycystic Ovary Syndrome as a Metabolic Disease," *Nature Reviews Endocrinology* 21, no. 4 (2025): 230–244, https://doi.org/10.1038/s41574-024-01057-w.

2. R. Singh, S. Kaur, S. Yadav, and S. Bhatia, "Gonadotropins as Pharmacological Agents in Assisted Reproductive Technology and Polycystic Ovary Syndrome," *Trends in Endocrinology & Metabolism* 34, no. 4 (2023): 194–215, https://doi.org/10.1016/j.tem.2023.02.002.

3. Z. Cai, R. Zhang, R. Liu, L. Zhao, and L. Zhou, "Plumbagin Ameliorates Ferroptosis of Ovarian Granulosa Cells in Polycystic Ovary Syndrome by Down-regulating SLC7A5 m6A Methylation Modification through Inhibition of YTHDF1," *Journal of Ovarian Research* 18, no. 1 (2025): 115, https://doi.org/10.1186/s13048-025-01700-8.

4. Y. Li, H. Song, J. Xu, et al., "TIGAR Relieves PCOS by Inhibiting Granulosa Cell Apoptosis and Oxidative Stress through Activating Nrf2," *Molecular and Cellular Endocrinology* 594 (2024): 112381, https://doi.org/10.1016/j.mce.2024.112381.

5. R. Ji, F. Jia, X. Chen, Y. Gao, and J. Yang, "Carnosol Inhibits KGN Cells Oxidative Stress and Apoptosis and Attenuates Polycystic Ovary Syndrome Phenotypes in Mice through Keap1-Mediated Nrf2/ HO -1 Activation," *Phytotherapy Research* 37, no. 4 (2023): 1405–1421, https://doi.org/10.1002/ptr.7749.

6. S. Gao, J. Wang, L. Wei, et al., "Trehalosemodulates OVRAS to Improve Oxidative Stress and Apoptosis in KGN Cells and Ovaries of PCOS Mice," *Journal of Ovarian Research* 17, no. 1 (2024): 11, https://doi.org/10.1186/s13048-023-01337-5.

7. S. Novakovic, V. Jakovljevic, N. Jovic, et al., "Exploring the Antioxidative Effects of Ginger and Cinnamon: a Comprehensive Review of Evidence and Molecular Mechanisms Involved in Polycystic Ovary Syndrome

(PCOS) and Other Oxidative Stress-Related Disorders," *Antioxidants (Basel)* 13, no. 4 (2024): 392, https://doi.org/10.3390/antiox13040392.

8. Y. J. Chien, C. C. Cho, Y. T. Hung, et al., "Gut Microbiota Modulation and Anti-Obesity Potential of Epigallocatechin-3-Gallate-Quercetin-Rutin against High-Fat Diet-Induced Obesity in Rats," *Life (Basel)* 15, no. 8 (2025): 1331, https://doi.org/10.3390/life15081331.

9. H. Jiang, J. Liu, Z. Xu, et al., "Quercetin Alleviates Acute Pancreatitis by Modulating Glycolysis and Mitochondrial Function via PFKFB3 Inhibition," *Cellular and Molecular Life Sciences* 82, no. 1 (2025): 311, https://doi.org/10.1007/s00018-025-05845-z.

10. A. Neisy, F. Zal, A. Seghatoleslam, and S. Alaee, "Amelioration by Quercetin of Insulin Resistance and Uterine GLUT4 and ERa Gene Expression in Rats with Polycystic Ovary Syndrome (PCOS)," *Reproduction, Fertility and Development* 31, no. 2 (2019): 315–323, https://doi.org/10.1071/rd18222.

11. P. Su, C. Chen, L. Pang, K. Wu, and Y. Sun, "Effects of Quercetin on Polycystic Ovary Syndrome in Animal Models: a Systematic Review and Meta-analysis," *Reproductive Biology and Endocrinology* 22, no. 1 (2024): 46, https://doi.org/10.1186/s12958-024-01220-y.

12. D. Bień, A. Lange, A. Matuszewski, et al., "Biocompatibility and Antioxidant Effects of Hydroxyapatite-quercetin Composites: in Vitro and in Ovo Studies," *Scientific Reports* 15, no. 1 (2025): 31532, https://doi.org/10.1038/s41598-025-17387-2.

13. X. Yang, B. Wang, H. Zeng, et al., "A Modified Polydopamine Nanoparticle Loaded with Melatonin for Synergistic ROS Scavenging and Anti-Inflammatory Effects in the Treatment of Dry Eye Disease," *Advanced Healthcare Materials* 14, no. 7 (2025): 2404372, https://doi.org/10.1002/adhm.202404372.

14. S. Yan, Z. Gao, J. Ding, et al., "Nanocomposites Based on Nanoceria Regulate the Immune Microenvironment for the Treatment of Polycystic Ovary Syndrome," *Journal of Nanobiotechnology* 21, no. 1 (2023): 412, https://doi.org/10.1186/s12951-023-02182-w.

15. K. Hu, X. Li, Z. Tan, and Y. Shi, "Simple ROS-responsive Micelles Loaded Shikonin for Efficient Ovarian Cancer Targeting Therapy by Disrupting Intracellular Redox Homeostasis," *European Journal of Pharmaceutics and Biopharmaceutics* 204 (2024): 114525, https://doi.org/10.1016/j.ejpb.2024.114525.

16. W. Peng, T. Zhou, L. Hu, et al., "Autonomous Activation of a Gated Chemiluminescent Photosensitizer Enables Targeted Photodynamic Therapy in Tumor Cells," *Journal of the American Chemical Society* 147, no. 31 (2025): 27822–27834, https://doi.org/10.1021/jacs.5c06761.

17. F. Jia, B. Yu, J. Li, et al., "Supramolecular Nano-Assembly of Caffeate-Strengthened Phenylboronic Ester with Multistep ROS Scavenging Ability for Targeted Therapy of Acute Kidney Injury," *Advanced Healthcare Materials* 12, no. 30 (2023): 2301615, https://doi.org/10.1002/adhm.202301615.

18. R. Zhou, Z. Bao, X. Chen, et al., "Prevention of Hepatic Ischemia-reperfusion Injury by Reactive Oxygen Species-responsive Nanozymes," *Journal of Controlled Release* 385 (2025): 114057, https://doi.org/10.1016/j.jconrel.2025.114057.

19. R. Liu, E. Zhao, Y. Wang, et al., "Silk-engineered Bioactive Nanoparticles for Targeted Alleviation of Acute Inflammatory Disease via Macrophage Reprogramming," *Journal of Nanobiotechnology* 23, no. 1 (2025): 11, https://doi.org/10.1186/s12951-024-03055-6.

20. Y. Huang, H. Xie, L. Liu, H. Zhao, B. Li, and F. Zhang, "Bioactive ROS-responsive Nanotherapeutics Attenuate Intermittent Hypoxia-induced Cognitive Impairment via NRF2/KEAP1/HO-1 Signaling," *Neurochemistry International* 188 (2025): 105997, https://doi.org/10.1016/j.neuint.2025.105997.

21. J. Liao, Z. Zhu, J. Zou, et al., "Macrophage Membrane-Biomimetic Multi-Layered Nanoparticles Targeting Synovial Angiogenesis for Osteoarthritis Therapy," *Advanced Healthcare Materials* 14, no. 2 (2025): 2401985, https://doi.org/10.1002/adhm.202401985.

22. Y. Gan, W. Xie, M. Wang, et al., "Cancer Cell Membrane-camouflaged CuPt Nanoalloy Boosts Chemotherapy of Cisplatin Prodrug to Enhance Anticancer Effect and Reverse Cisplatin Resistance of Tumor," *Materials Today Bio* 24 (2024): 100941, https://doi.org/10.1016/j.mtbio.2023.100941.

23. X. Wang, F. Zhang, N. Li, et al., "Fabrication of Macrophage-membrane Coated Functionalized ROS-responsive Thiolated Chitosan-based Nanoparticles to Attenuate Atherosclerosis: Investigation on Diabetic Hyperlipidaemia-induced Mice Model," *International Journal of Biological Macromolecules* 321, no. Pt 3 (2025): 145880, https://doi.org/10.1016/j.ijbiomac.2025.145880.

24. X. Lin, Q.-F. Meng, Y. Pan, et al., "Inhalable Macrophage Membrane-Camouflaged Hyperbranched Polymeric Nanoparticles for Acute Lung Injury Treatment," *Nano Letters* 25, no. 34 (2025): 13003–13013, https://doi.org/10.1021/acs.nanolett.5c03271.

25. K. N. Panchal, S. Mutalik, and J. Manikkath, "Biomimetic Nanoparticle-driven Strategies for Targeted Drug Delivery in Glioblastoma," *Journal of Nanoparticle Research* 26, no. 8 (2024): 192, https://doi.org/10.1007/s11051-024-06104-1.

26. S. H. Lee, M. K. Gupta, J. B. Bang, H. Bae, and H. J. Sung, "Current Progress in Reactive Oxygen Species (ROS)-Responsive Materials for Biomedical Applications," *Advanced Healthcare Materials* 2, no. 6 (2013): 908–915, https://doi.org/10.1002/adhm.201200423.

27. Y. Murata, T. Kotani, H. Ohnishi, and T. Matozaki, "The CD47-SIRP Signalling System: Its Physiological Roles and Therapeutic Application," *Journal of Biochemistry* 155, no. 6 (2014): 335–344, https://doi.org/10.1093/jb/mvu017.

28. X. Su, M. Su, E. Guo, et al., "Tissue-Resident Macrophage Membrane-Coated Nanomedicine for Targeted Tumor Therapy," *ACS Nano* 19 (2025): 26296, https://doi.org/10.1016/j.biomaterials.2024.123072.

29. X. Su, M. Su, E. Guo, et al., "Tissue-Resident Macrophage Membrane-Coated Nanomedicine for Targeted Tumor Therapy," *ACS Nano* 19, no. 29 (2025): 26296–26319, https://doi.org/10.1021/acsnano.5c04463.

30. J.-J. Xu, C.-Z. Yan, Z.-Q. Liu, et al., "Vitexin Reduced the Dihydrotestosterone (DHT)-induced Fibrosis in KGN Cells by Regulating the NR4A1/NLRP3 Pathway," *The Journal of Steroid Biochemistry and Molecular Biology* 257 (2025): 106927, https://doi.org/10.1016/j.jsbmb.2025.106927.

31. Y. Feng, L. Wu, and J. Liu, "Systematic Investigation of the Potential Multi-target Pharmacological Mechanisms of Astragaloside IV in Polycystic Ovary Syndrome via Network Pharmacology and in Vivo/in Vitro Experiments," *Naunyn-Schmiedeberg's Archives of Pharmacology* (2025), https://doi.org/10.1007/s00210-025-04667-x.

32. R. Ji, S. Wang, X. Chen, et al., "Platycodin D Ameliorates Polycystic Ovary Syndrome-induced Ovarian Damage by Upregulating CD44 to Attenuate Ferroptosis," *Free Radical Biology and Medicine* 224 (2024): 707–722, https://doi.org/10.1016/j.freeradbiomed.2024.09.033.

33. Y. Cai, Z. Zhang, C. Liu, et al., "Size-dependent Translocation and Lymphatic Transportation of Polymeric Nanocarriers post Intraperitoneal Administration," *Journal of Controlled Release* 376 (2024): 553–565, https://doi.org/10.1016/j.jconrel.2024.10.032.

34. J. Liang, Y. Gao, Z. Feng, B. Zhang, Z. Na, and D. Li, "Reactive Oxygen Species and Ovarian Diseases: Antioxidant Strategies," *Redox Biology* 62 (2023): 102659, https://doi.org/10.1016/j.redox.2023.102659.

35. F. Ebrahimi, S. Rostami, S. Nekoonam, Z. Rashidi, A. Sobhani, and F. Amidi, "The Effect of Astaxanthin and Metformin on Oxidative Stress in Granulosa Cells of BALB C Mouse Model of Polycystic Ovary Syndrome," *Reproductive Sciences* 28, no. 10 (2021): 2807–2815, https://doi.org/10.1007/s43032-021-00577-4.

36. M. A. Butt, S. Tabassum, R. S. Hardy, and M. M. Kiyani, "Mechanistic Insight into Nanomedicine for Polycystic Ovary Syndrome," *Molecular Biology Reports* 52, no. 1 (2025): 618, https://doi.org/10.1007/s11033-025-10709-7.

37. M. Shi, X. Li, L. Xing, et al., "Polycystic Ovary Syndrome and the Potential for Nanomaterial-Based Drug Delivery in Therapy of this

Disease," *Pharmaceutics* 16, no. 12 (2024): 1556, https://doi.org/10.3390/pharmaceutics16121556.

38. P. Niziński, A. Hawrył, P. Polak, et al., "Potential of Quercetin as a Promising Therapeutic Agent against Type 2 Diabetes," *Molecules (Basel, Switzerland)* 30, no. 15 (2025): 3096, https://doi.org/10.3390/molecules30153096.

39. K. Kandemir, M. Tomas, D. J. McClements, and E. Capanoglu, "Recent Advances on the Improvement of Quercetin Bioavailability," *Trends in Food Science & Technology* 119 (2022): 192–200, https://doi.org/10.1016/j.tifs.2021.11.032.

40. R. M. Mesgin, V. Nejati, S. P. Talatapeh, Z. Imani, and J. Rezaie, "Nanoparticles for Polycystic Ovary Syndrome (PCOS) Therapy: Exosomes and Synthetic Nanoparticles, Challenges and Opportunities," *Cell Biochemistry and Function* 43, no. 9 (2025): 70114, https://doi.org/10.1002/cbf.70114.

41. K. Liu, X. Ma, Y. Zhang, L. Zhao, and Y. Shi, "Precision Delivery of Pretreated Macrophage-membrane-coated Pt Nanoclusters for Improving Alzheimer's Disease-Like Cognitive Dysfunction Induced by Porphyromonas gingivalis," *Biomaterials* 319 (2025): 123211, https://doi.org/10.1016/j.biomaterials.2025.123211.

42. H. Ma, Y. Li, H. Shi, et al., "Berberine-Calcium Alginate-coated Macrophage Membrane-derived Nanovesicles for the Oral Treatment of Ulcerative Colitis," *International Journal of Biological Macromolecules* 294 (2025): 139114, https://doi.org/10.1016/j.ijbiomac.2024.139114.

43. B. Yao, J. Zhang, Z. Chen, et al., "Macrophage-membrane-engineered NIR II Biomimetic Nanomaterials for Enhanced Synergistic Chemo-photothermal Immunotherapy in Cancer Treatment," *Colloids and Surfaces B: Biointerfaces* 253 (2025): 114759, https://doi.org/10.1016/j.colsurfb.2025.114759.

44. S. Liu, B. Li, Q. Yang, et al., "Pathology-Driven Design of a Biomimetic Ferromagnetic Nanomedicine for Dual-Mode Treatment of Ulcerative Colitis and Colitis-Associated Colorectal Cancer," *Advanced Materials* 38 (2025): 14413, https://doi.org/10.1002/adma.202514413.

45. J. Liao, L. Lu, X. Chu, et al., "Cell Membrane Coated Nanoparticles: Cutting-edge Drug Delivery Systems for Osteoporosis Therapy," *Nanoscale* 16, no. 17 (2024): 8236–8255, https://doi.org/10.1039/d3nr06264c.

46. X. Lu, Z. Chen, C. Yi, et al., "An Anti-CD47 Antibody Binds to a Distinct Epitope in a Novel Metal Ion-dependent Manner to Minimize Cross-linking of Red Blood Cells," *Journal of Biological Chemistry* 301, no. 8 (2025): 110420, https://doi.org/10.1016/j.jbc.2025.110420.

47. N. Hasan, M. Imran, D. Jain, et al., "Advanced Targeted Drug Delivery by Bioengineered White Blood Cell-membrane Camouflaged Nanoparticulate Delivery Nanostructures," *Environmental Research* 238, no. Pt 1 (2023): 117007, https://doi.org/10.1016/j.envres.2023.117007.

48. S. Gupta and P. P. Sarangi, "Inflammation Driven Metabolic Regulation and Adaptation in Macrophages," *Clinical Immunology* 246 (2023): 109216, https://doi.org/10.1016/j.clim.2022.109216.

49. D. Tang, Y. Wang, A. Wijaya, et al., "ROS-responsive Biomimetic Nanoparticles for Potential Application in Targeted Anti-atherosclerosis," *Regenerative Biomaterials* 8, no. 4 (2021): rbab033, https://doi.org/10.1093/rb/rbab033.

50. S. K. Cho, K. Lee, J. H. Woo, and J. H. Choi, "Macrophages Promote Ovarian Cancer-Mesothelial Cell Adhesion by Upregulation of ITGA2 and VEGFC in Mesothelial Cells," *Cells* 12, no. 3 (2023): 384, https://doi.org/10.3390/cells12030384.

51. S. Yang, B. He, C. He, et al., "Red Blood Cell Membrane-Camouflaged Reduction-Responsive Polyethylenimine-Based Nanoparticles for Enhanced Antitumor Efficacy of Antisense Oligonucleotides," *Molecular Pharmaceutics* 22, no. 9 (2025): 5458–5472, https://doi.org/10.1021/acs.molpharmaceut.5c00412.

52. J. Nai, J. Zhang, J. Li, et al., "Macrophage Membrane- and cRGD-functionalized Thermosensitive Liposomes Combined with CPP to Realize Precise siRNA Delivery into Tumor Cells," *Molecular Therapy Nucleic Acids* 27 (2022): 349–362, https://doi.org/10.1016/j.omtn.2021.12.016.

53. D. Liu, A. Yang, Y. Li, et al., "Targeted Delivery of Rosuvastatin Enhances Treatment of Hyperhomocysteinemia-induced Atherosclerosis Using Macrophage Membrane-coated Nanoparticles," *Journal of Pharmaceutical Analysis* 14, no. 9 (2024): 100937, https://doi.org/10.1016/j.jpha.2024.01.005.

54. X. Wang, Z. Zhang, Y. Qi, et al., "Study of the Uptake Mechanism of Two Small Extracellular Vesicle Subtypes by Granulosa Cells," *Animal Reproduction Science* 270 (2024): 107576, https://doi.org/10.1016/j.anireprosci.2024.107576.

55. A. Abdulova, M. Purelku, H. Sahin, and G. Tanrıverdi, "Human Ovarian Granulosa Cells Use Clathrin-mediated Endocytosis for LDL Uptake: Immunocytochemical and Electron Microscopic Study," *Ultrastructural Pathology* 47, no. 4 (2023): 241–252, https://doi.org/10.1080/01913123.2023.2200532.

56. J. Zhao, F. Jia, J. Li, et al., "Sprayable Reactive Oxygen Species-Responsive Hydrogel Coatings Restore Endothelial Barrier Integrity for Functional Vascular Healing," *ACS Nano* 19, no. 23 (2025): 21757–21774, https://doi.org/10.1021/acsnano.5c05477.

57. M. Izadi, M. E. Rezvani, A. Aliabadi, M. Karimi, and B. Aflatoonian, "Mesenchymal Stem Cells-derived Exosomes as a Promising New Approach for the Treatment of Infertility Caused by Polycystic Ovary Syndrome," *Frontiers in Pharmacology* 13 (2022): 1021581, https://doi.org/10.3389/fphar.2022.1021581.

58. F. Nikmard, E. Hosseini, M. Bakhtiyari, M. Ashrafi, F. Amidi, and R. Aflatoonian, "The Boosting Effects of Melatonin on the Expression of Related Genes to Oocyte Maturation and Antioxidant Pathways: a Polycystic Ovary Syndrome- mouse Model," *Journal of Ovarian Research* 15, no. 1 (2022): 11, https://doi.org/10.1186/s13048-022-00946-w.

59. Y. Lin, Y. Zhang, X. Ding, et al., "Chlorogenic Acid Mitigates DHEA-induced Oxidative Stress in Granulosa Cells and Alleviates Ferroptosis via the NF-κB Signaling Pathway in PCOS," *European Journal of Pharmacology* 1002 (2025): 177870, https://doi.org/10.1016/j.ejphar.2025.177870.

60. X. Teng, Z. Wang, and X. Wang, "Enhancing Angiogenesis and Inhibiting Apoptosis: Evaluating the Therapeutic Efficacy of Bone Marrow Mesenchymal Stem Cell-derived Exosomes in a DHEA-induced PCOS Mouse Model," *Journal of Ovarian Research* 17, no. 1 (2024): 121, https://doi.org/10.1186/s13048-024-01445-w.

61. Q. Zhang, M. Liu, J. Zhang, et al., "Macrophage MAPK7/AhR/STAT3 Signaling Mediates Mitochondrial ROS Burst and Enterohepatic Inflammatory Responses Induced by Deoxynivalenol Relevant to Low-Dose Exposure in Children," *Environmental Science & Technology* 58, no. 42 (2024): 18589–18602, https://doi.org/10.1021/acs.est.4c05875.

62. Y. Wang, D. Han, Y. Huang, et al., "Oral Administration of punicalagin Attenuates Imiquimod-Induced Psoriasis by Reducing ROS Generation and Inflammation via MAPK / ERK and NF-κB Signaling Pathways," *Phytotherapy Research* 38, no. 2 (2024): 713–726, https://doi.org/10.1002/ptr.8071.

63. Z. Zhou, Z. Tu, J. Zhang, et al., "Follicular Fluid-Derived Exosomal MicroRNA-18b-5p Regulates PTEN-Mediated PI3K/Akt/mTOR Signaling Pathway to Inhibit Polycystic Ovary Syndrome Development," *Molecular Neurobiology* 59, no. 4 (2022): 2520–2531, https://doi.org/10.1007/s12035-021-02714-1.

64. L. Luobin, H. Wanxin, G. Yingxin, et al., "Nanomedicine-induced Programmed Cell Death in Cancer Therapy: Mechanisms and Perspectives," *Cell Death Discovery* 10, no. 1 (2024): 386, https://doi.org/10.1038/s41420-024-02121-0.

65. B. Li, J. Rao, W. Hu, et al., "Adropin as a Therapeutic Candidate for HFpEF: Evidence of Oxidative Stress Mitigation via Nrf2/HO-1 Signaling," *Lipids in Health and Disease* 24, no. 1 (2025): 273, https://doi.org/10.1186/s12944-025-02703-6.

66. W. Yang, J. Qiu, J. Zi, et al., "Effect of Rhei Radix Et Rhizome on Treatment of Polycystic Ovary Syndrome by Regulating PI3K/AKT Pathway and Targeting EGFR/ALB in Rats," *Journal of Ethnopharmacology* 338, no. 1 (2025): 119020, https://doi.org/10.1016/j.jep.2024.119020.

67. M. Liu, H. Zhu, X. Zhou, J. Duan, Y. Shen, and A. Zhang, "Cell-Free Fat Extract Prevents Diminished Ovarian Reserve by Inhibiting Granulosa Cell Senescence," *Stem Cell Research & Therapy* 16, no. 1 (2025): 269, https://doi.org/10.1186/s13287-025-04383-6.

68. X. Liang, Y. Zhang, C. Wang, et al., "ROS-responsive Death Receptor 5 Fusion Protein Nano-delivery System Enhances Myocardial Ischemia-reperfusion Injury Protection," *Materials Today Bio* 32 (2025): 101899, https://doi.org/10.1016/j.mtbio.2025.101899.

69. W. Zhang, M. Zuo, J. Lu, and Y. Wang, "Adiponectin Reduces Embryonic Loss Rate and Ameliorates Trophoblast Apoptosis in Early Pregnancy of Mice with Polycystic Ovary Syndrome by Affecting the AMPK/PI3K/Akt/FoxO3a Signaling Pathway," *Reproductive Sciences* 27, no. 12 (2020): 2232–2241, https://doi.org/10.1007/s43032-020-00237-z.

Supporting Information

Additional supporting information can be found online in the Supporting Information section.

Supporting File: adhm70957-sup-0001-SuppMat.pdf.